# RESEARCH ACTIVITIES III
# Department of Electronic Structure

## III-A Photochemical Synthesis of Exotic Organo-Metallic Clusters with Magnetic Properties

We have succeeded to generate cluster molecular magnets of $(Co)_x(CH)_y(CH_2)_z$. Although information on the structure of the cluster molecules is not enough, *ab initio* molecular orbital calculation of $(Co)_4(CH)_4(CH_2)_4$ at B3LYP/6-31G level has suggested a deformed cubane type structure that is composed of four cobalt atoms bridged with CH carbon atoms and $CH_2$ groups coordinate with the cobalt atoms. Photochemical treatment of $C_5H_5Co(CO)_2$ in dichloromethane generated cobaltocene ($C_5H_5CoC_5H_5$) and $(Co)_x(CH)_y(CH_2)_z$ with keeping the chemical balance of Co atoms. The latter species became magnets at temperatures lower than 5 K in a matrix of cobaltocene and its derivatives, showing a hysteresis curve characteristic of single molecular magnets: free rotation for the inversion of external magnetic field across zero field and making their cavities wider suited for rotation. Photochemical treatment of $Co_4(CO)_{12}$ in dichloromethane produced $(CoCHCH_2)_4$. The black solid product exhibited residual cohesive magnetization with a blocking temperature of 16 K. Electronic structure of these compounds is also very interesting in relation to the origin of ferromagnetism in such cluster molecular magnets.

### III-A-1 Photochemical Generation of Cluster Molecular Magnets: $(CoCHCH_2)_4$

**HINO, Kazuyuki[1]; KOSUGI, Kentaroh; SEKIYA, Hiroshi[1]; HOSOKOSHI, Yuko; INOUE, Katsuya; NISHI, Nobuyuki**
*([1]Kyushu Univ.)*

Development of molecular level magnets is one of the recent topics in nanoscience and nanotechnology. In order to make magnetic molecules with high spin quantum numbers, we forcus our attention to cobalt atoms composed of 7 electrons in 3d orbitals and 2 electrons in the 4s orbital. A carbonyl compound $Co_4(CO)_{12}$ was dissolved in dichloromethane solution and high pressure mercury lamp with UV cut-off filter irradiated the solution in a closed glass vessel with a gas exhaust valve. The product solution was mixed with a large amount of anthracene for embedding product molecules in anthracene matrix. The solution was introduced into a new mass spectrometer (see AR2000, III-A-2) through a liquid chromatograph pump and the solute species were deposited as a helical belt on a titanium drum that was rotating and translating in a sample chamber under vacuum. On the opposite side of the drum, after the rotation of 180°, the solute species were photoionized and desorped by 355 nm laser pulses. Then the ions were introduced to a reflectron mass spectrometer. The mass number of the main product was 344, and assigned to $(CoCHCH_2)_4$. The solid formed in the reaction vessel was filtrated by using a Millipore filter with a pore size of 0.2 μm. Magnetic properties of the solid photoproducts were measured with a SQUID magnetometer (Quantum Design MPMS-7S).

Figure 1-a shows $\chi_g T$ change of the photoproducts against temperatue, where $\chi_g$ is mass succeptibility. It is composed of two kinds of magnetic species. One exhibits antiferromagnetic behavior: the $\chi_g T$ value increases with increasing temperature, while the other behaves ferromagnetically at temperatures lower than 30 K. The former component is highly soluble in dichloromethane, whereas the latter is prone to precipitate in the solution. The $\chi_g T$ change of the washed precipitate shows a maximum value of $3.8 \times 10^{-2}$ emu $g^{-1}$ K at 20 K. Figure 1-b shows magnetization curves upon temperature cooling with or without magnetic field at 10 Oe. The field cooling aligns the molecular magnets along the magnetic field at temperatures lower than the blocking temperature, 16 K, where the zero-field cooling shows maximum magnetization with reducing magnetization at lower temperatures due to random orientation of the magnets. Figure 1-c shows a hysteresis curve of the magnetization. Although both the residual magnetization and the coercive force are small as compared with pure metallic magnets, the hydrogenated carbon-cobalt clusters with 4 cobalt atoms behave as magnets at temperatures lower than 16 K. In order to raise the blocking temperature, we have to increase the number of cobalt atoms up to several tens in the clusters with keeping cubane type frameworks. The origin of generating a high spin angular momentum is expected to the heavy charge transfer from cobalt atoms to carbon atoms on the basis of our molecular orbital calculation and XPS studies.

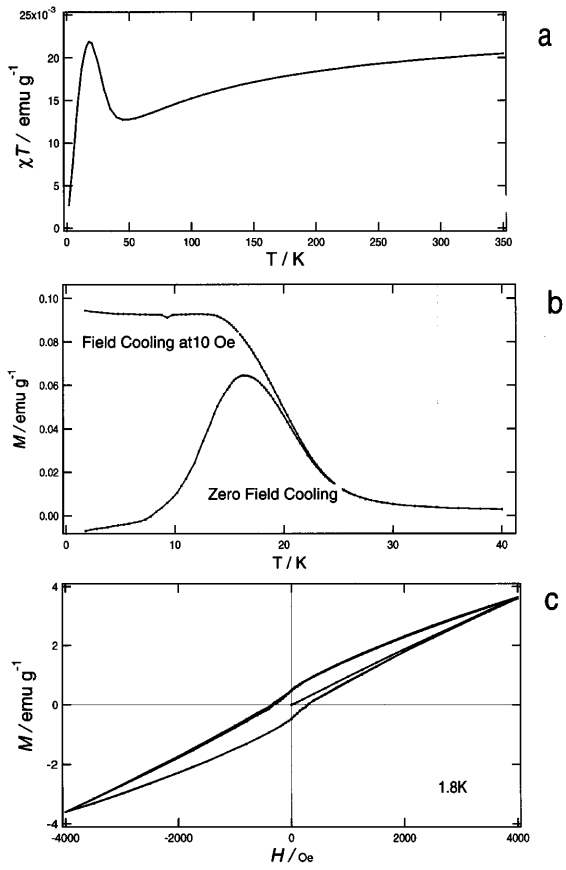


**Figure 1.** Magnetic properties of photoproducts from $Co_4(CO)_{12}$ and $CH_2Cl_2$; a: $\chi_g T$ as a function of temperature, b: Magnetization upon field cooling at 10 Oe (upper curve) and on zero field cooling (lower trace), c: hysteresis curve.

### III-A-2 Magnetic Behavior of Single Molecular Magnets (Hydrated Carbon-Cobalt Clusters) Isolated in a Glassy Matrix of Cobaltocene and Its Derivatives Generated from Photochemical Reaction of $(C_5H_5)Co(CO)_2$ in Dichloromethane

**HINO, Kazuyuki[1]; KOSUGI, Kentaroh; SEKIYA, Hiroshi[1]; HOSOKOSHI, Yuko; INOUE, Katsuya; NISHI, Nobuyuki**
*([1]Kyushu Univ.)*

Photochemical reaction of $(C_5H_5)Co(CO)_2$ in dichloromethane exhibited release of CO and the following condensation reaction producing cobaltocence, $(C_5H_5)Co(C_5H_5)$, and $Co_x(CH)_y(CH_2)_z$. The latter cluster products could be generated by the photochemical reaction of solvated cobalt atoms with releasing Cl atoms from reaction intermediates. Secondary reactions also produce bicobaltocene and related compounds, $(C_5H_5)Co(C_5H_4–C_5H_4)Co(C_5H_5)$, $(C_5H_5–C_5H_4)Co(C_5H_4–C_5H_5)$, $(C_5H_5)Co(C_5H_4–C_5H_5)$, making the solid products glassy. Very fine particles were observed by a scanning electron microscope as spherical balls of the order of several hundred nm. Although the concentration of the hydrogenated carbon-cobalt clusters, $Co_x(CH)_y(CH_2)_z$, is higher in the filtrate solution, the fine particles also contains the clusters as much as approximately 5% of cobaltocene matrices as found by the laser ionization/desorption mass spectrometry of the solid products.

The $\chi_g T$ change of the fine particles behaved as a superparamagnetic material showing beautifully flat plateau at a level of 0.01 emu $g^{-1}$ K in the temperature range from 50 K to 350 K. At the lower temperatures it increases exhibiting a maximum at 6 K as high as 0.05 emu $g^{-1}$ K. The blocking temperature of 6 K was obtained from the ac magnetization measurement. The hysteresis curve is shown in Figure 1-a. One can see the following very intersting features characterisic of single molecular magnets in a matrix composed of bulky molecules: 1; the magnetization loop obtained after several cycles of external field modulation is located much higher than the initial magnetization rise curve, 2; at 0 (±10) Oe the magnetization decreases very quickly . These features indicate that the alighnment and the rotation of magnetic molecules following the change of the external magnetic field make the space for the magnetic molecules suited for free rotation. The orientational alignment of the spin axes of the magnets became much better when the magnets have experienced rotations forced by the change of the external magnetic field. The blocking temperature is much lower than that observed for the matrix free bulk compound as shown in III-A-1, while the residual magnetic moment at 0 Oe is much larger than the bulk material.

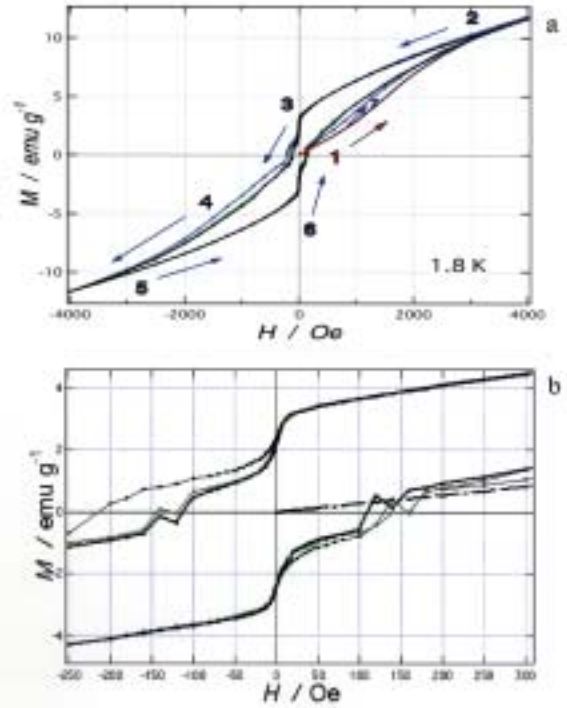


**Figure 1.** a: Magnetic moment hysteresis observed for $Co_x(CH)_y(CH_2)_z$ magnets in a matrix composed of $(C_5H_5)Co(C_5H_5)$ and its derivatives. Note that the initial magnetization curve is located lower than that the second magnetization loop. b: Expanded view around low magnetic field.

### III-A-3 Photochemical Generation of High Spin Clusters in Solution: (Cyclopentadienyl-Vanadium)$_m$O$_n$

**HINO, Kazuyuki[1]; INOKUCHI, Yoshiya; KOSUGI, Kentaroh; SEKIYA, Hiroshi[1]; HOSOKOSHI, Yuko;**

**INOUE, Katsuya; NISHI, Nobuyuki**
*([1]Kyushu Univ.)*

Organometallic clusters containing oxygen atoms, $(CpV)_mO_n$ (Cp = $C_5H_5$), are generated by photochemical reaction of $CpV(CO)_4$ in $CH_2Cl_2$ solution under control of oxygen contents. Mass spectra of single batch reactions exhibit strong signals assigned to low mass oxide clusters; $(CpV)_4O_4$, $(CpV)_5O_6$, and $(CpV)_6O_n$ ($n$ = 6~8). Successive addition of reactant solution into the photochemical reaction vessel shows the addition of $(CpV)_m$, to the low mass oxide clusters producing $(CpV)_mO_n$ ($m >> n$ = 4~7). The magnetic susceptibility ($\chi_g$) of the mixture of the former low mass products shows antiferromagnetic behavior, while that of the latter high mass products is as high as $4.6 \times 10^{-4}$ $cm^3$ $g^{-1}$ at 10 K and the additional part due to high mass products behaves ferromagnetically at temperatures higher than 70 K.

# III-B States of Neutral and Ionic Molecular Associates in Solutions

States of molecular associates particularly in aqueous solutions are of great importance in understanding the role of molecules in living organisms. We found that any ideally mixed state cannot be seen in protic-protic mixtures such as water-alcohol, water-acetic acid, and alcohol-acetic acid systems on the molecular level at solute molar fractions ($\chi_A$) higher than 0.001. In such a system, solute-solute association is highly favored resulting in microscopic phase separation. Here we demonstrate that aprotic solvent such as acetonitrile can produce ideally mixed state(s) for acetic acid.

## III-B-1 States of Molecular Associates in Binary Mixtures of Acetic Acid with Aprotic Polar Solvents: the Nature of Mixture States at Molecular Levels

**NAKABAYASHI, Takakazu; NISHI, Nobuyuki**

The structures and dynamics of liquids have received much attention over the past three decades. Our recent studies of Raman spectroscopy have shown that binary solutions of acetic acid with protic solvents do not get ideally mixed on the molecular level at acetic acid molar fractions ($\chi_A$) higher than 0.001. In aprotic polar solvents, however, the C=O stretching band of acetic acid shows the mixing ratio dependence different from that in protic solvents. Temperature dependence of the Raman spectra of the acetic acid and acetonitrile binary solution at $\chi_A$ = 0.01 is shown in Figure 1. As the temperature grows, the 1725 $cm^{-1}$ band shifts to a lower-wavenumber, while the 1754 $cm^{-1}$ band shifts to a higher-wavenumber. The intensity of the 1754 $cm^{-1}$ band relative to that of the 1725 $cm^{-1}$ band becomes larger with increasing temperature. The relative intensity between the two bands is independent of the acid concentration. These results suggest that the two bands arise from two types of acetic acid monomers in different environment. To examine the two different types of acetic acid monomers in acetonitrile, ab initio calculations are carried out with self-consistent reaction field method (B3LYP/6311++G** level). The dipole moment of a dipolar molecule becomes larger on going from the gas phase to the acetonitrile solution. Thus the C=O bond of the acetic acid monomer becomes longer and its C=O stretching mode shifts to a lower-wavenumber in acetonitrile. However, the C=O mode of the cyclic dimer in Figure 1 shows a higher-wavenumber shift in acetonitrile, because of the decrease in the C=O···H–C interaction. These results indicate that the C=O band of the cyclic dimer shifts to a lower-wavenumber and that of the non-complexed acetic acid monomer shifts to a higher-wavenumber as the solute-solvent electrostatic interaction decreases. The dielectric constant decreases with increasing temperature, which means that the electrostatic interaction becomes weaker as the temperature grows. Thus, the positional changes in Figure 1 can be explained when the 1725 and 1754 $cm^{-1}$ bands are assigned to the cyclic dimer and the non-complexed acetic acid monomer, respectively. Such two bands are also observed in other aprotic polar solvents such as 1,4-dioxane, indicating that the two types of acetic acid monomers are also exist in other aprotic polar solvents. It is therefore concluded that acetic acid molecules preferentially exist as the monomeric forms in the aprotic polar solvents. This means that ideally-mixed states at molecular levels exist in the binary solutions of acetic acid and the aprotic polar solvents when the mole fraction of acet ic acid is small. From several spectroscopic studies on other binary solutions, the mixing rules at molecular levels may be proposed as follows: protic-protic binary mixtures do not easily become ideally-mixed states even when the mixing ratio is large, while ideally-mixed states at molecular levels appear in protic-aprotic polar binary mixtures at low concentrations of the protic solvent.

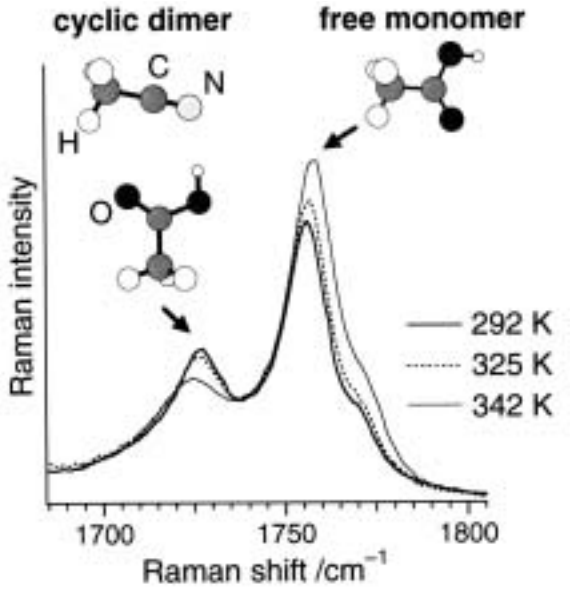


**Figure 1.** Temperature dependence of the C=O bands of the acetic acid and acetonitrile mixture.

### III-B-2 Structure of Clusters in Methanol-Water Binary Solutions Studied by Mass Spectrometry and X-Ray Diffraction

**TAKAMUKU, Toshiyuki[1]; YAMAGUCHI, Toshio[2]; ASATO, Masaki[3]; MATSUMOTO, Masaki[3]; NISHI, Nobuyuki**
*(Saga Univ.[1]; Fukuoka Univ.[2]; Kyushu Univ.[3])*

[*Z. Naturforsch., A: Phys. Sci.* **55**, 513 (2000)]

The structure of clusters in methanol-water solutions in its dependence on the methanol mole fraction $\chi_M$ has been investigated by mass spectrometry on clusters isolated from submicron droplets by adiabatic expansion in vacuum and by X-ray diffraction on the bulk binary solutions. The mass spectra have shown that the average hydration number, ($n_m$), of *m*-mer methanol clusters decreases with increasing $\chi_M$, accompanied by two inflection points at $\chi_M$ = ~0.3 and ~0.7. The X-ray diffraction data have revealed a similar change in the number of hydrogen bonds per water and/or methanol oxygen atom at ~2.8 Å. On the basis of both results, most likely models of clusters formed in the binary solutions are proposed: at $0 < \chi_M < 0.3$ tetrahedral-like water clusters is the main species, at $0.3 < \chi_M < 0.7$ chain clusters of methanol molecules gradually evolve with increasing methanol content, and finery at at $\chi_M > 0.7$ the chain clusters of methanol molecules become predominant. The present results are compared with clusters previously found in ethanol-water binary solutions and discussed in relation to anomalies of the heat of mixing of methanol-water binary solutions.

# III-C Ultrafast Dynamics and Structural Changes of Aromatic Cation Radicals

Release of an electron from a neutral molecule by photons induces eminent structural changes of the molecule and reorientation of solvent molecules. In particular, polar solvents stabilize the newly born cation due to Coulombic interaction causing thermal excitation of surrounding solvents and the cation. Geminate recombination of the ejected electrons and the parent cations is also expected. We have studied the ultrafast dynamics upon photoionization of aromatic molecules by time-resolved absorption and Raman spectroscopic techniques.

### III-C-1 Ultrafast Relaxation Dynamics of Aromatic Cation Radicals Following Photoionization

**NAKABAYASHI, Takakazu; KAMO, Satoshi[1]; SAKURAGI, Hirochika[1]; NISHI, Nobuyuki**
*([1]Univ. Tsukuba and IMS)*

Photoionization in condensed phases has been a subject of interest for many years. Charge-pair generation, recombination, solvation and vibrational relaxation processes as well as cation structural changes can occur after photoionization of aromatic molecules in solvents. In the previous study, solvation and vibrational relaxation processes occurring on a picosecond time scale are discussed.[1)] In the present study, we have measured femtosecond time-resolved absorption spectra of aromatic cation radicals (naphthalene, biphenyl, and 1,4-diphenylbutadiene) in nonpolar and polar solvents and discussed the dynamics of the photoionization in the subpico- to picosecond time range. Figure 1 shows the time-resolved absorption spectra of the cation radical of naphthalene in cyclohexane. The broad absorption decays in several picoseconds, which can be attributable to the geminate recombination of the electrons with their parent cation radicals. The induced absorption in acetonitrile, however, shows the temporal profile different from that in cyclohexane. As shown in Figure 2, the absorption intensity first decreases in the subpicosecond range, and then increases on a 10–20 ps time scale. The absorption around 700 nm also shifts to a lower-wavelength with the delay time. The picosecond increase in the absorption intensity is observed in all the region of 600–740 nm. The temporal profile observed in ethyl acetate is similar to that in acetonitrile. The subpicosecond decay components can be ascribed to the geminate recombination of the unsolvated cation radical, which competes with the reorganization of solvent molecules. To our best knowledge, it is the first report to observe the ultrafast geminate recombination

of unsolvated aromatic cation radicals in polar solvents. The picosecond increase in the absorption intensity is observed in all the cation radicals treated, suggesting that the picosecond relaxation process increasing the cation absorption intensity occurs after the photoionization of the aromatic molecules. The time scale of the change in the absorption intensity is the same as that of the vibrational relaxation, while the intensity rise does not correlate with the dielectric relaxation time. The picosecond rise is significantly observed in highly polar solvents forming strong solvent–solute interactions. From these observations, we propose the model that the thermal excitation of the solvent shell disturbs the solvation structure of the cation radical, which causes the change in the cation absorption intensity. Contrary to the generally accepted view, this result suggests that the cation radical formed by the multi-photon ionization is solvated on a 10–20 ps time scale, because of the thermal excitation of the neighboring solvent shell.

**Reference**

1) T. Nakabayashi, S. Kamo, H. Sakuragi and N. Nishi, *J. Phys. Chem. A* in press.

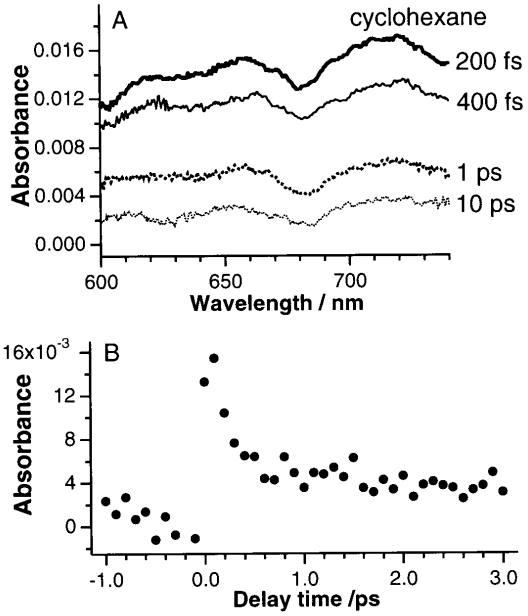


**Figure 1.** (A) Femtosecond time-resolved absorption spectra of naphthalene cation radical in cyclohexane. (B) Temporal profile of the absorbance due to naphthalene cation radical in cyclohexane at 685 nm.

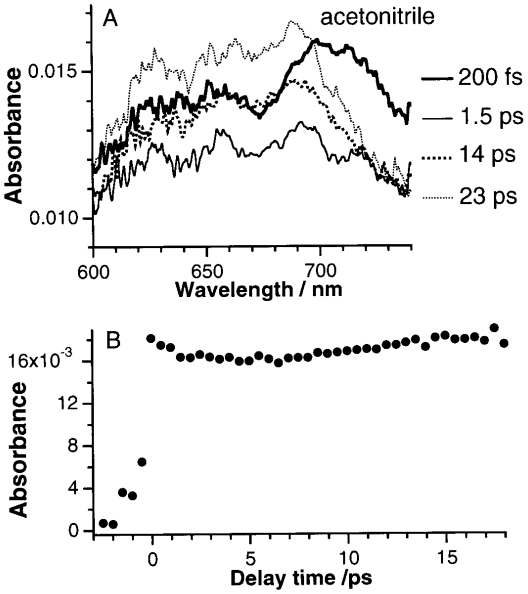


**Figure 2.** (A) Femtosecond time-resolved absorption spectra of naphthalene cation radical in acetonitrile. (B) Temporal profile of the absorbance due to naphthalene cation radical in acetonitrile at 685 nm.

# III-D Spectroscopic and Dynamical Studies on Charge Delocalization and Charge Transfer in Molecular Cluster Ions

Electron deficiency of molecular cluster cations can attract electron rich groups or atoms exhibiting a charge transfer or a charge resonance interaction in the clusters. These interactions cause dynamical changes of structures such as proton transfer or ion-core switching in hot cluster ions.

## III-D-1 Photodissociation Spectroscopy of Benzene Cluster Ions in Ultraviolet and Infrared Regions. Static and Dynamic Behavior of Positive Charge in Cluster Ions

**INOKUCHI, Yoshiya; NISHI, Nobuyuki**

[*J. Chem. Phys.* **114**, 7059 (2001)]

Photodissociation spectroscopy is applied to benzene cluster ions in ultraviolet and infrared regions. In the ultraviolet photodissociation spectrum of $(C_6H_6)_3^+$, a characteristic broad band emerges at 255 nm. This band is assigned to a $\pi^* \leftarrow \pi$ transition of a solvent benzene molecule that exists in the trimer. This is in accord with a previous model of the ion cluster with a dimer ion core and a solvent benzene molecule. Infrared photodissociation spectra of $(C_6H_6)_n^+$ ($n$ = 3–5) show a sharp band at 3066 $cm^{-1}$. The band is attributed to a C–H stretching vibration of the dimer ion core. The infrared spectra of $(C_6H_6)_n^+$ ($n$ = 3–5) are fitted to model spectra produced by combining the C–H stretching bands of the dimer ion core and the solvent benzene molecule. Infrared photodissociation spectra of mixed benzene trimer ions with one or two benzene-$d_6$ molecules demonstrate that there is no correlation between the excited dimer ion core site in the trimer and the photofragment dimer ion species. This result implies that a dimer ion core switching occurs in photoexcited vibrational states prior to the dissociation.

### III-D-2 Infrared Photodissociation Spectroscopy of Protonated Formic Acid-Water Binary Clusters, $H^+\cdot(HCOOH)_n\cdot H_2O$ ($n$ = 1–5). Spectroscopic Evidence of Ion Core Switch Model

**INOKUCHI, Yoshiya; NISHI, Nobuyuki**

Static and dynamic features of the positive charge distribution in cluster ions are very important, because they are related very much with the charge transportation in condensed phases. In this study, we apply infrared (IR) photodissociation spectroscopy to protonated formic acid-water binary clusters, $H^+\cdot(HCOOH)_n\cdot H_2O$ ($n$ = 1–5). We also investigate ab initio molecular orbital calculations to obtain optimized structures and theoretical IR spectra. By comparing the observed IR photodissociation spectra with the calculated ones, we discuss structures and an ion core switching process in these clusters.

The IR photodissociation spectra of $H^+\cdot(HCOOH)_n\cdot H_2O$ ($n$ = 1–5) are measured by using an ion guide spectrometer with two quadrupole mass filters. The MO calculations are performed by using the Gaussian 98 program package at B3LYP/6-31G(d,p) level.

Figure 1 shows the IR photodissociation spectra in 3100–3800 $cm^{-1}$ region. For $n$ = 1–3, there are two maxima in the IR spectra. We assign the low-frequency bands to free OH stretching vibrations of the formic acid molecules. The high-frequency bands are ascribed to asymmetric OH stretching vibrations of the water molecules. For $n$ = 4, the high-frequency band disappears from the spectrum. For $n$ = 5, no sharp bands exist in the spectrum. Because the free OH stretching band of water (the high-frequency band) is not observed for $n$ = 4 and 5, the $H_2O$ molecule is in the periphery of the clusters for $n \leq 3$, but it is located in an inner position of the clusters for $n > 3$. Furthermore, the theoretical calculations predict that the ion-core switch occurs from $HCOOH_2^+$ to $H_3O^+$ between $n$ = 3 and 4. The most stable structures of $n$ = 4 and 5 predicted by the theoretical calculations are also shown in Figure 1. In the clusters of $n$ = 4 and 5, the ion core is $H_3O^+$. The $H_3O^+$ ion core is thought to be unstable due to the lower proton affinity of water (165 kcal/mol) than that of formic acid (177.3 kcal/mol). However, the formic acid molecules surround and stabilize the $H_3O^+$ ion cores in the clusters. In summary, the ion core switch really occurs from $HCOOH_2^+$ to $H_3O^+$ between $n$ = 3 and 4 in $H^+\cdot(HCOOH)_n\cdot H_2O$.

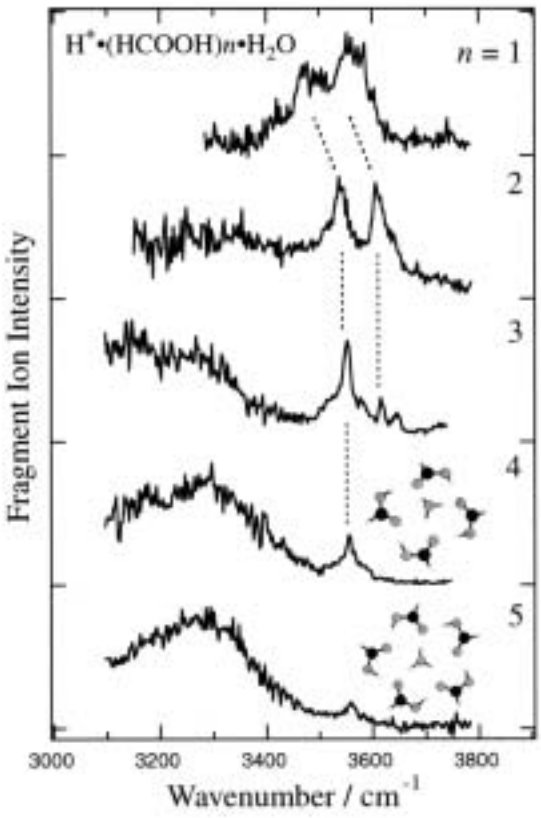


**Figure 1.**

### III-D-3 Charge Transfer Interaction in Acetic Acid-Benzene Cation Complex

**KOSUGI, Kentaroh; INOKUCHI, Yoshiya; NISHI, Nobuyuki**

[*J. Chem. Phys.* **114**, 4805 (2001)]

Geometrical and electronic structures of acetic acid-benzene cation complex, $(CH_3COOH)\cdot(C_6H_6)^+$, are studied experimentally and theoretically. Experimentally, a vibrational spectrum of $(CH_3COOH)\cdot(C_6H_6)^+$ in the supersonic jet is measured in the 3000-3680 $cm^{-1}$ region using an ion-trap photodissociation spectrometer. An electronic spectrum is also observed with this spectrometer in the 12000–29600 $cm^{-1}$ region. Theoretically, ab initio molecular orbital calculations are performed for geometry optimization and evaluation of vibrational frequencies and electronic transition energies. The frequency of the strong band (3577 $cm^{-1}$) is close to that of the O–H stretching vibration of acetic acid and the weak one is located at 3617 $cm^{-1}$. On the basis of geometry optimizations and frequency calculations, the strong band is assigned to the O–H stretching vibration of the *cis*-isomer of acetic acid in

the hydrogen-bonded complex (horizontal *cis*-isomer). The weak one is assigned to the vertical *trans*-isomer where the *trans*-isomer of acetic acid interacts with the π-electron system of the benzene cation. The weakness of the high frequency band in the photodissociation spectrum is attributed to the binding energy larger than the photon energy injected. Only hot vertical *trans*-isomers can be dissociated by the IR excitation. The electronic spectrum exhibits two bands with intensity maxima at 17500 $cm^{-1}$ and 24500 $cm^{-1}$. The calculations of electronic excitation energies and oscillator strengths suggest that charge transfer bands of the vertical *trans*-isomer can be observed in this region in addition to a local excitation band of the horizontal *cis*-isomer. We assign the 17500 $cm^{-1}$ band to the charge transfer transition of the vertical *trans*-isomer and the 24500 $cm^{-1}$ band to the π-π transition of the horizontal *cis*-isomer. The calculations also suggest that the charge transfer is induced through the intermolecular C···O=C bond formed between a carbon atom of benzene and the carbonyl oxygen atom of acetic acid.

# III–E Synthesis and Characterization of Metal Clusters

Recently, metal clusters consisted of several tens or several hundreds of metal atoms have gained much attention as new nano-scaled materials because their properties are significantly different from the corresponding bulk and behave in a size-dependent manner. To exploit a synthetic method of metal clusters while controlling their size in an atomic level is a challenging task which will help us to understand the size-dependent properties of the clusters and open up many possibilities for the wide range of applications. We have addressed the issue by adopting the following approaches: 1) Chemical synthesis of the clusters in the presence of molecular capsules, which work as templates and stabilizers for the clusters and 2) characterization of the clusters by mass spectrometry. Our goal is to reveal the origin of the size-specific chemical reactions occurring on the surface of metal clusters.

## III-E-1 Development of Mass Spectrometer for Metal Clusters Dispersed in Liquid Phase

**NEGISHI, Yuichi; TSUKUDA, Tatsuya**

Mass spectrometry is a powerful diagnostics for the metal clusters because it provides useful information complementary to that obtained from the conventional characterization by TEM; the cluster size and composition can, in principle, be characterized in an atomic resolution. We have constructed an apparatus consisting of electrospray ionization (ESI) source and time-of-flight (TOF) mass spectrometer with a reflectron as shown in Figure 1. Liquid sample containing the metal clusters is pumped through a fused silica capillary, whose end is supported in a stainless steel needle. Charged aerosol droplets are electrosprayed by means of an electrical potential between the needle tip and a counter electrode (+3–5 kV). The cluster ions contained in the droplets are evaporated into the gas phase and further desolvated by passing through a heated capillary. A portion of the ion flow is skimmed and introduced into the acceleration region of the TOF mass spectrometer. Then, the ions are extracted in the direction perpendicular to the initial beam by applying a pulsed voltage of ~15 kV to a set of grids. The ions are stirred by several sets of ion optics and detected by either a microchannel plate (MCP) detector located at the end of the flight path of ~3.2 m (low-resolution mode) or another MCP detector with a center hole after reflected by the coaxial reflectron (high-resolution mode). Figure 2 shows a typical ESI mass spectrum of tetra-*n*-octylammonium bromide obtained in the high-resolution mode.

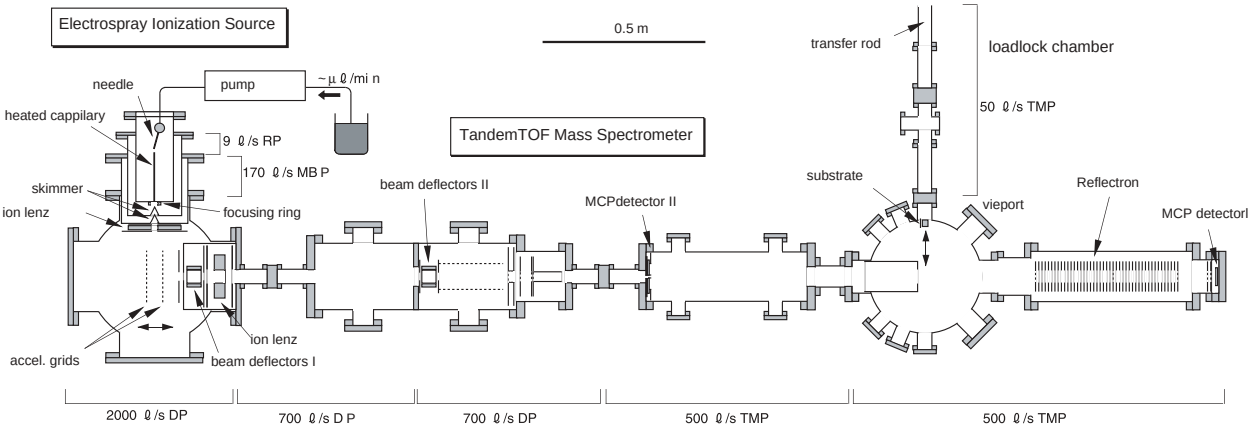


**Figure 1.** Schematic diagram of the experimental apparatus.

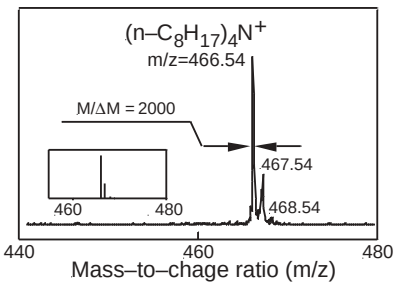


**Figure 2.** The positive-ion ESI mass spectrum of tetra-*n*-octylammonium bromide run in a methanol mobile phase. Inset shows the isotopic distribution of $(n\text{-}C_8H_{17})_4N^+$ calculated from the natural abundance. Mass resolution of $m/\Delta m$ ~ 2000 is routinely achieved in the high-resolution mode.

## III-E-2 Mass Spectroscopic Characterization of Transition Metal Clusters Encapsulated by PAMAM Dendrimers

**NEGISHI, Yuichi; TSUKUDA, Tatsuya**

Synthesis of metal nanoclusters using dendrimers as "nanotemplates" has been one of the most exciting topics in recent cluster chemistry.[1)] The dendrimers are hyper-branched polymers, which are almost spherical in shape, sterically crowded on the exterior, and somewhat hollow on the interior. A strategy proposed for preparation of the dendrimer-encapsulated nanoparticles is rather simple:[1)] Introduction of metal ions into the internal cavity of dendrimers followed by chemical reduction of the metal ions.

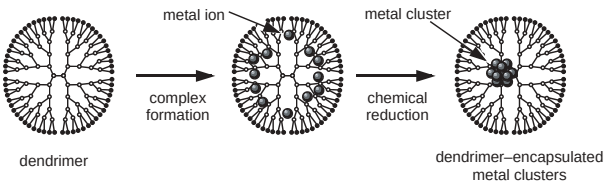


We have followed the synthetic procedures by ESI mass spectrometry. Figure 1A shows ESI mass spectra of OH-terminated poly(amido)amine dendrimers with a third generation (G3-OH). A series of prominent peaks discernible in Figure 1A are assigned to the multiply charged molecular ions of G3-OH with the ideal structure. Mass peaks interspersed between them are due to the G3-OH molecules with missing arms, which are present as contamination in the sample. Figure 1B shows mass spectrum of the complexes of G3-OH and silver ions, which are prepared by mixing 16-fold molar excess of $AgNO_3$. Clusters containing up to 10 Ag ions are recognizable whereas the larger clusters are not because of overlapping of the mass peaks due to the heterogeneity of the G3-OH sample. The chemical reduction of these complexes by $NaBH_4$ or hydrazine results in the formation of Ag clusters stabilized by G3-OH. The ESI spectrum obtained for the clusters is essentially the same with that of free G3-OH (Figure 1C). This observation suggests that the Ag clusters are passivated weakly by several G3-OH which are easily removed during the ES processes. It is conceivable that the aggregation of Ag(0) atoms proceeds outside the dendrimer because of low density of G3-OH surface and/or low partition coefficient of the Ag ions. Following studies are now underway in our group: 1) Purification of the dendrimers by gel permeation chromatography and 2) synthesis of nanoclusters by using dendrimers with higher generations having more dense surfaces.

**Reference**

1) R. M. Crooks *et al.*, *Topics in Current Chemistry* **212**, 81 (2001) and references therein.

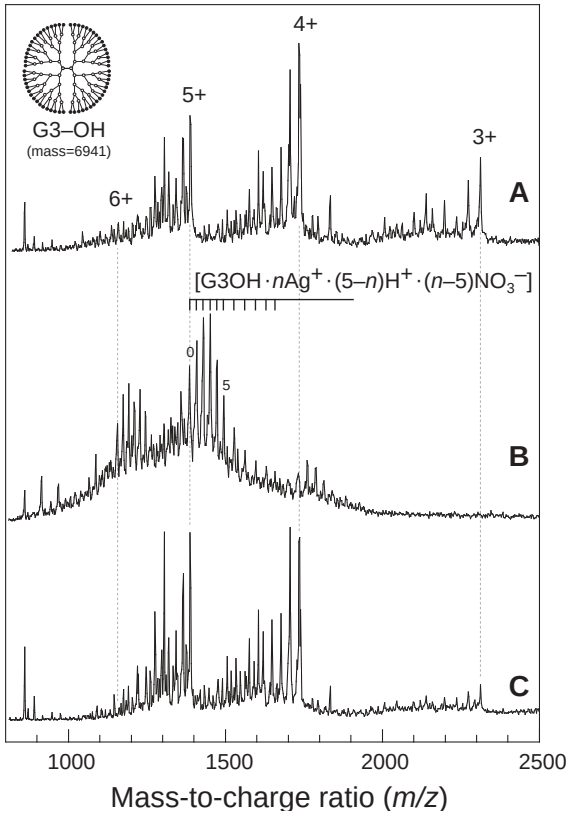


**Figure 1.** The ESI mass spectra of A) G3-OH PAMAM dendrimers, B) complexes between G3-OH and silver ions, C) silver clusters stabilized by G3-OH.

# III-F Geometric and Electronic Structures of Negatively-Charged Molecular Clusters

The geometric and electronic structures of negatively-charged molecular clusters are among the most fundamental issues in cluster science: How do the molecular aggregates trap an excess electron and how do the structures evolve with cluster size? Among the systems studied so far, negatively-charged clusters of carbon dioxide, $(CO_2)_n^-$, have been a prototype system to address these issues. Some intriguing phenomena have been observed in the previous photoelectron spectroscopic studies of $(CO_2)_n^-$ (*Chem. Phys. Lett.* **268**, 429 (1997)): 1) Existence of distinct isomers having different anionic cores of $CO_2^-$ and $C_2O_4^-$ ("electronic isomers"), 2) switching of the anionic core from $CO_2^-$ to $C_2O_4^-$ and vice versa at $n$ = 7 and 14, respectively ("core switching"), 3) spontaneous interconversion between $CO_2^-\cdot(CO_2)_5 \rightleftarrows C_2O_4^-\cdot(CO_2)_4$ at $n$ = 6 ("electronic isomerization"). We have studied the structures of isomers for small $(CO_2)_n^-$ clusters and their isomerization processes by ab initio calculations. Structural evolution of $(CO_2)_n^-$ has been investigated by mass spectrometry.

## III-F-1 *Ab initio* Study of $CO_2^-\cdot CO_2 \rightleftarrows C_2O_4^-$ Isomerization

**SAEKI, Morihisa; TSUKUDA, Tatsuya; NAGATA, Takashi[1]**
*([1]Univ. Tokyo)*

[*Chem. Phys. Lett.* in press]

The potential energy surface relevant to the isomerization of $(CO_2)_2^-$ has been investigated by *ab initio* calculations including effects of electron correlation. The surface plotted against appropriate

angle parameters shows two shallow minima and a deep valley, which correspond to $CO_2^-{\cdot}CO_2$ ($C_{2v}$), $CO_2^-{\cdot}CO_2$ ($C_s$) and $C_2O_4^-$ ($D_{2d}$) structures, respectively. The transition states for the $C_{2v} \rightleftarrows C_s \rightleftarrows D_{2d}$ interconversion are located well below the $CO_2^-$ + $CO_2$ dissociation limit, which allows $(CO_2)_2^-$ with sufficient internal energies to fluctuate among the isomeric forms. The calculations have also revealed quantitatively the behavior of the excess charge flow during the $CO_2^-{\cdot}CO_2 \rightleftarrows C_2O_4^-$ electronic isomerization.

**Reference**

1) M. Saeki, T. Tsukuda, S. Iwata and T. Nagata, *J. Chem. Phys.* **111**, 6333 (1999).

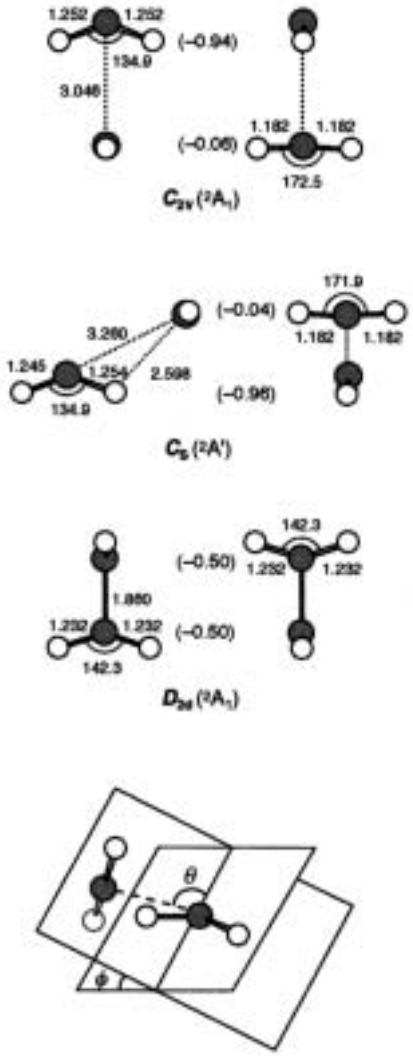


**Figure 1.** Top and side views of the geometries of $(CO_2)_2^-$ isomers optimized at the MP2/6-31+G* level (taken from reference 1). The digits in parentheses represent the Mulliken gross populations on the $CO_2$ moieties. Bond lengths and bond angles are given in Å and degrees. Also given in the figure are definitions of angle parameters θ and ϕ to describe the intermolecular motion during isomerization.

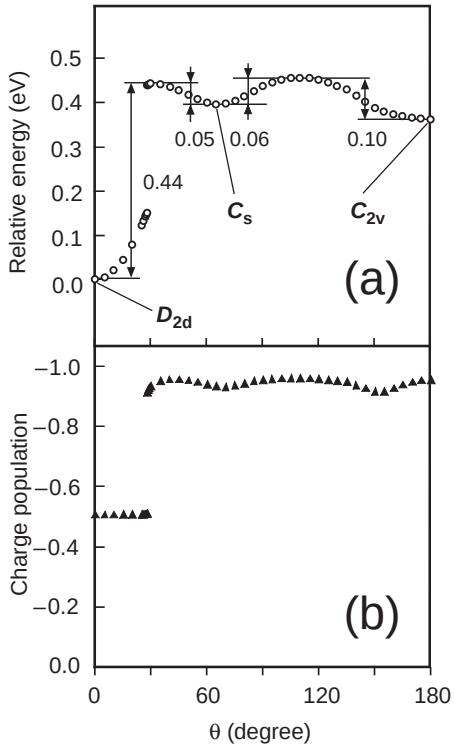


**Figure 2.** Potential profile along the minimum-energy path for the $(CO_2)_2^-$ isomerization (panel a) and the charge population at each transient structure (panel b) plotted against angle θ. The numbers in the panel (a) represent the barrier heights for the isomerization in electron volts. The charge population corresponds to the Mulliken gross populations on the $CO_2$ unit carrying a larger excess charge.

## III-F-2 *Ab initio* Study of $(CO_2)_n^-$: Structures and Stabilities of Isomers

**SAEKI, Morihisa; TSUKUDA, Tatsuya; NAGATA, Takashi[1]**

*([1]Univ. Tokyo)*

[*Chem. Phys. Lett.* **340**, 376 (2001)]

The geometrical structures and stabilities of $(CO_2)_n^-$ with the size range $3 \le n \le 6$ are investigated by *ab initio* calculations including effects of electron correlation. The calculations have shown that the structures of $(CO_2)_n^-$ can be formulated by either $CO_2^-{\cdot}(CO_2)_{n-1}$ or $C_2O_4^-{\cdot}(CO_2)_{n-2}$, and that the geometry of $(CO_2)_2^-$ dimer remains more or less in all the optimized structures. In all the sizes investigated in the present study, the most stable isomers are of the $C_2O_4^-{\cdot}(CO_2)_{n-2}$ form, being consistent with the results obtained in the photoelectron spectroscopic studies.[1)]

**Reference**

1) T. Tsukuda, M. A. Johnson and T. Nagata, *Chem. Phys. Lett.* **268**, 429 (1997).

## III-F-3 Structural Evolution of Large $(CO_2)_n^-$ Clusters as Studied by Mass Spectrometry

**NEGISHI, Yuichi; NAGATA, Takashi[1]; TSUKUDA, Tatsuya**

*([1]Univ. Tokyo)*

Negatively-charged clusters of $CO_2$ are generated by electron-impact ionized free jet expansion and analyzed by mass spectrometry. Figure 1 shows typical mass spectra of $(CO_2)_n^-$ covering the size range up to $n \sim 1000$ ($m/z \sim 44000$). Abrupt intensity drops in otherwise smooth distributions are observed in the size range of $n \leq 150$, whereas a series of humps are discernible in the spectra recorded in the mass range $n \geq 150$. Weak but distinct intensity anomalies are also observed in the distributions of the $(CO_2)_n^+$ cluster cations in the size range of $n \leq 150$, while oscillatory structures similar to those of $(CO_2)_n^-$ are observed in the $n \geq 150$ range. These comparisons suggest that the magic numbers associated with the small $(CO_2)_n^-$ clusters ($n \leq 150$) reflect intrinsic stabilities of ions, and that the intensity distributions of larger $(CO_2)_n^-$ cluster are mostly determined by the abundance of neutral $CO_2$ clusters. To find reasonable structural models for $(CO_2)_n^-$, the magic numbers are compared with the sizes predicted from the Mackay icosahedral packing sequence. For $n \leq 150$, the magic numbers observed experimentally ($n$ = 14, 52, and 146) are close to the sizes predicted for icosahedral structures having complete layers ($n$ = 13, 55, 147). These similarities suggest icosahedron-like structures for small $(CO_2)_n^-$ clusters which are somewhat deformed due to the presence of anionic cores. In contrast, the distributions for larger clusters cannot be explained by icosahedral structure model, being consistent rather with the cubic structures for neutral clusters in the $n \gg 55$ range.[1)]

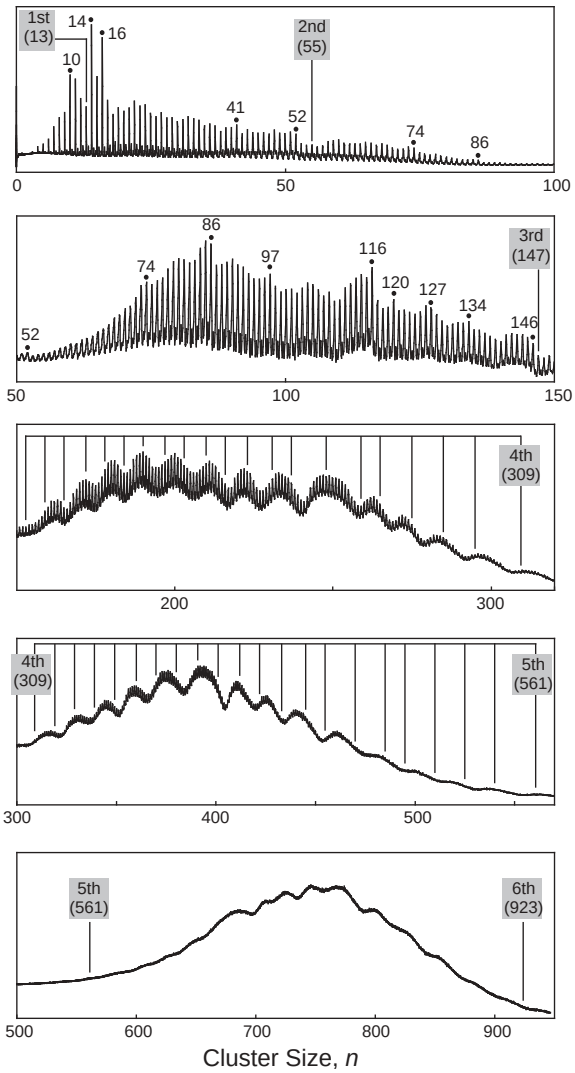


**Figure 1.** Typical mass spectra of $(CO_2)_n^-$. Bars in the figure represent the cluster sizes at which additional subshell structures are closed around the complete icosahedron structures. Note that these mass spectra are recorded while changing the deflection voltage so that the cluster ions of a given size range can be detected simultaneously.

**Reference**

1) J.-B. Maillet, A. Boutin and A. H. Fuchs, *J. Chem. Phys.* **111**, 2095 (1999).

# III-G Spectroscopy and Dynamics of Vibrationally Excited Molecules and Clusters

This research group is studying structure and dynamics of molecules and clusters by two-color double resonance spectroscopy. New spectroscopic methods will also be developed to observe the higher vibrational state under collision-free condition.

## III-G-1 Picosecond Time-Resolved Infrared Spectra of Photo-Excited Phenol-$(NH_3)_3$ Cluster

**ISHIUCHI, Shun-ichi; SAKAI, Makoto; DAIGOKU, Kota[1]; UEDA, Tadashi; YAMANAKA, Takaya; HASHIMOTO, Kenro[1]; FUJII, Masaaki**
*([1]Tokyo Metropolitan Univ. and ACT-JST)*

[*Chem. Phys. Lett.* in press]

Picosecond time-resolved IR spectra of phenol-$(NH_3)_3$ have been measured by UV-IR-UV ion dip spectroscopy for the first time (Figure 1). It was found that the time-evolution of two vibrational bands at 3180 $cm^{-1}$ and 3250 $cm^{-1}$ is different from each other. The results show that two transient species are generated from the photo-excited phenol-$(NH_3)_3$ cluster. From *ab initio* calculation, the transient species are assigned to two isomers of $(NH_3)_2NH_4$ (see Special Research Activity for more detail).

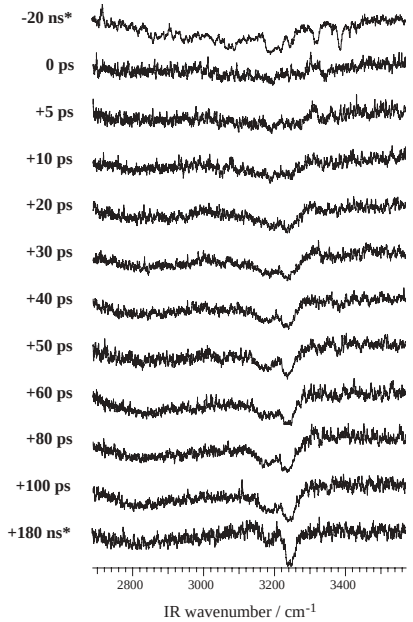


**Figure 1.** Picosecond time-resolved UV-IR-UV ion dip spectra of the transient species from the electronically excited PhOH-$(NH_3)_3$ which was observed by fixing the first laser $\nu_{UV}$ to the low vibronic band in the $S_1$ state of PhOH–$(NH_3)_3$ (281.49 nm) and monitoring $(NH_3)_2NH_4^+$ due to the ionization laser $\nu_{ION}$ (355 nm). Times indicated at the left side of each spectrum mean the delay times between $\nu_{UV}$ and the IR probe laser $\nu_{IR}$. The spectra whose delay times are –20 ns and +180 ns (indicated by *) are obtained by nanosecond laser system, which have been reported in the previous paper (*Chem. Phys. Lett.* **322**, 27 (2000)).

## III-G-2 Structure of Hydrogen-Bonded Clusters of 7-Azaindole Studied by IR Dip Spectroscopy and Ab Initio Molecular Orbital Calculation

**YOKOYAMA, Hiroshi[1]; WATANABE, Hidekazu[2]; OMI, Takuichiro[1]; ISHIUCHI, Shun-ichi; FUJII, Masaaki**
*([1]Waseda Univ. and PRESTO; [2]AIST Shikoku, Natl. Inst. Adv. Ind. Sci. Tech.)*

[*J. Phys. Chem.* in press]

The IR spectrum of 7-azaindole monomer, 7-azaindole reactive and nonreactive dimers, and 7-azaindole $(H_2O)_n$ ($n$ = 1–3) clusters in a supersonic jet from 2600 $cm^{-1}$ to 3800 $cm^{-1}$ have been measured using IR dip spectroscopy. The vibrational transitions in the ground state were clearly observed and were assigned to the CH and NH stretching vibrations of 7-azaindole and the OH stretching vibrations of water molecules in the clusters. The observed IR spectra of 7-azaindole monomer and 7-azaindole$(H_2O)_n$ ($n$ = 1–3) clusters were compared to theoretical ones obtained by *ab initio* MO calculations. From a comparison, it is concluded that 7-azaindole$(H_2O)_n$ ($n$ = 1–3) clusters have a ring structure due to a cyclic hydrogen-bond network. This conclusion is consistent with an analysis based on high-resolution spectroscopy. Similarly, the IR dip spectrum suggests that the 7-Azaindole reactive dimer has a cyclic hydrogen-bond network, forming a symmetric planer structure. It is strongly suggested from the IR spectrum and the ab initio calculations that the nonreactive dimer contains a water molecule between 7-azaindole molecules.

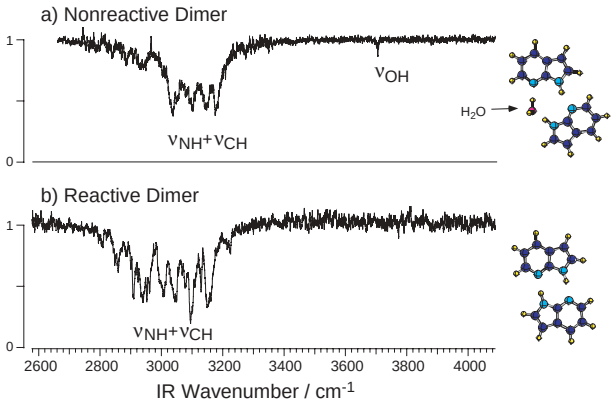


**Figure 1.** IR dip spectrum of (a) 7-azaindole reactive dimer and (b) nonreactive dimer. The structures concluded from the observed IR spectrum and *ab initio* calculations are also shown.

### III-G-3 Structures of Carbazole-$(H_2O)_n$ ($n$ = 1–3) Clusters Studied by IR Dip Spectroscopy and a Quantum Chemical Calculation

**SAKAI, Makoto; DAIGOKU, Kota[1]; ISHIUCHI, Shun-ichi; SAEKI, Morihisa; HASHIMOTO, Kenro[1]; FUJII, Masaaki**
*([1]Tokyo Metropolitan Univ. and ACT-JST)*

[*J. Phys. Chem.* in press]

The IR spectra of carbazole and carbazole-$(H_2O)_n$ ($n$ = 1–3) clusters in a supersonic jet have been measured by IR dip spectroscopy. The spectra show clear vibrational structures of both the monomer and the clusters in the 2900–3800 $cm^{-1}$ frequency region. The observed vibrational bands are assigned to the NH stretch of carbazole and the OH stretches of $H_2O$ molecules in the clusters. The geometries and IR spectra of carbazole-$(H_2O)_n$ clusters were calculated at the HF/6-31G and B3LYP/6-31++G(d,p) levels. From a comparison of the observed and calculated IR spectra, the structures of the cluster have been determined.

### III-G-4 Structure of 1-Naphthol/Alcohol Clusters Studied by IR Dip Spectroscopy and Ab Initio Molecular Orbital Calculations

**SAEKI, Morihisa; ISHIUCHI, Shun-ichi; SAKAI, Makoto; FUJII, Masaaki**

[*J. Phys. Chem.* in press]

The structures of 1-naphthol/alcohol clusters, 1-NpOH$(ROH)_n$ ($n$ = 1–3; ROH = MeOH, EtOH, and t-BuOH), have been investigated by resonant two-photon ionization (R2PI) spectroscopy and ion-detected IR dip spectroscopy. Based on the calculated spectra obtained by *ab initio* MO calculations, the spectra of 1-NpOH-$(MeOH)_n$ was analyzed. The analysis elucidated that 1-NpOH$(MeOH)_{2,3}$ was a ring structure. From a similarity of the spectral pattern, the structures of 1-NpOH-$(EtOH)_n$ and 1-NpOH(t-BuOH)$_n$ were also determined to be a ring conformation. From a frequency shift of the hydrogen-bonded OH stretching vibration, the hydrogen bonding is weakened by a steric hindrance due to an alkyl group of ROH. The difference in the solvation mechanism between 1-NpOH$(MeOH)_n$ and 1-NpOH-$(H_2O)_n$ is discussed.

### III-G-5 Structural and Dynamics of 9(10H)-Acridine and Its Hydrated Clusters. II Structual Characterization of Hydrogen-Bonding Networks

**MITSUI, Masaaki[1]; OHSHIMA, Yasuhiro[1]; ISHIUCHI, Shun-ichi[2]; SAKAI, Makoto; FUJII, Masaaki**
*([1]Kyoto Univ.; [2]GUAS)*

[*J. Phys. Chem. A* **104**, 8649 (2000)]

The present paper represents fluorescence-detected infrared measurements of 9(10H)-acridone (AD) and 10 of its fluorescent hydrated clusters, AD-$(H_2O)_n$ ($n$ = 1–5 and more), which have been performed by monitoring the fluorescence from their $^1(\pi,\pi^*)$ electronic origin transitions. In the $n$ = 1 and 2 clusters, free N–H stretching band has been identified in addition to O–H stretching bands characteristic to water molecules acting as single proton donors. As the next solvation step, the H-bonded O–H stretches are further developed in the red-shifted region and the N–H stretch becomes involved in the hydrogen-bonds for the $n$ = 3–5 clusters. For $n \geq 6$, more than one pair of double-donor O–H stretches appear. These spectral features are well correlated to the stepwise evolution in the hydrogen-bonding networks in AD-$(H_2O)_n$, which have been predicted by the $(\pi,\pi^*)$ spectral-shift analysis and DFT calculations presented in paper I: water units are bound to the C=O site for $n$ = 1 and 2, a single water chain bridges between the C=O and N–H sites above the AD aromatic rings for $n$ = 3–5, and water bridges become branched for ng 6 and probably form three-dimensional cages at higher aggregation levels. Differences in hydrogen-bonding topologies, stabilities, and dynamical behaviors among the conformers are discussed on the basis of the experimental observations, the DFT calculations, and comparison with other hydrated aromatic clusters.

### III-G-6 Internal Methyl Group Rotation in o-Cresol Studied by Pulsed Field Ionization – ZEKE Photoelectron Spectroscopy

**SUZUKI, Kazunari[1]; EMURA, Yuji[2]; ISHIUCHI, Shun-ichi[3]; FUJII, Masaaki**
*([1]YAMAHA; [2]Mitsui Chemical; [3]GUAS)*

[*J. Electron Spectrosc.* **108**, 13 (2000)]

Pulsed field ionization – ZEKE photoelectron spectroscopy and (1+1) R2PI spectroscopy have been applied to cis- and trans-o-cresol. The internal rotational structure in $S_1$ has been re-assigned for the cis-isomer, and the potential curve for the internal rotation has been determined. In the PFI-ZEKE spectra recorded via different internal rotational levels in the $S_1$ state, well-resolved low-frequency bands have been observed. The low-frequency bands are assigned to internal rotational motion of the methyl group in the cation. Level energies and relative transition intensities are reproduced well by a one-dimensional rotor model with a three-fold axis potential. Potential curves for the internal rotation have been determined for both cis- and trans-o-cresol cations. The barrier height for the internal rotation is different for the two isomers in the cation, while it becomes similar in $S_1$. Contributions of steric and electronic factors to the rotational barrier are discussed.

### III-G-7 Pulsed Field Ionization - ZEKE Spectroscopy of Cresoles and Their Aqueous Complex: Internal Rotation of Methyl Group and Intermolecular Vibrations

**SUZUKI, Kazunari[1]; ISHIUCHI, Shun-ichi[2]; FUJII, Masaaki**
*([1]YAMAHA; [2]GUAS)*

[*Faraday Discuss.* **115**, 229 (2000)]

Pulsed field ionization – ZEKE photoelectron spectroscopy and (1+1) R2PI spectroscopy have been applied to cis- and trans-m-cresol·$H_2O$ clusters. The internal rotational structure in $S_1$ has been re-assigned, and the potential curve has been determined for the cluster. The PFI-ZEKE spectra of cis- and trans-isomer show low-frequency bands up to 1000 $cm^{-1}$ above the adiabatic ionization potential $IP_0$. The low-frequency bands are assigned to the internal rotation of the methyl group, the intermolecular stretching and their combination bands in the m-cresol·$H_2O$ cluster cation. Level energies and relative transition intensities are reproduced well by a one-dimensional rotor model with a three-fold axis potential. Potential curves for the internal rotation have been determined for both cis- and trans-isomers of m-cresol·$H_2O$ cations. The effect of the cluster formation upon the internal methyl rotation, and interaction between the methyl rotation and the intermolecular vibration are discussed.

### III-G-8 Butterfly Vibration of the Tetrafluorobenzene Cation Studied by Pulsed Field Ionization – ZEKE Photoelectron Spectroscopy

**TAKAZAWA, Ken[1]; FUJII, Masaaki**
*([1]Natl. Res. Inst. Met.)*

[*J. Electron Spectrosc.* **112**, 241 (2000)]

The pulsed field ionization - ZEKE photoelectron spectroscopy has been applied to 1,2,4,5-tetra-fluorobenzene in a supersonic jet. The spectrum measured by selecting a specific vibronic level of butterfly vibrational mode in $S_1$ by the first laser shows well-resolved vibrational structure of the cation. A long progression has been assigned to the out-of-plane butterfly vibrational mode 11 with even quantum number in the cation. From the harmonisity and Franck-Condon factor, it has been concluded that the molecular structure of the tetrafluorobenzene cation is flat though that in $S_1$ is non-planer along the butterfly vibrational mode. The geometrical change upon ionization has been discussed in terms of the electronic structure.

# III-H Ultrafast Molecular Dynamics Studied by Time-Resolved Photoelectron Imaging

Femtosecond time-resolved photoelectron imaging is a novel experimental means to probe electronic and nuclear dynamics in real time. Since photoionization can occur from any part of the potential with any multiplicity, the method provides a universal method to follow dephasing and reaction processes.

## III-H-1 Photoelectron Imaging on Time-Dependent Molecular Alignment Created by a Femtosecond Laser Pulse

**TSUBOUCHI, Masaaki[1]; WHITAKER, Benjamin J.[2]; WANG, Li[3]; KOHGUCHI, Hiroshi, SUZUKI, Toshinori**

*([1]GUAS; [2]Univ. Leeds; [3]Dalian Inst. Chem. Phys.)*

[*Phys. Rev. Lett.* **86**, 4500 (2001)]

Rotational wave packet revivals on an excited electronic state of pyrazine have been measured by femtosecond time-resolved photoelectron imaging for the first time. The pump pulse (324 nm) excited pyrazine to the $S_1$ $0^0$ level, and the subsequent 401 nm probe pulse ionized this level by a two-photon process. Figure 1(a) shows a typical photoelectron image measured at a time delay of 30 ps between the pump and probe pulses. The pump and probe laser polarization are both vertical in the figure. The observed image consists of three major rings with different radii corresponding to the photoelectron kinetic energies of 37, 101, and 643 meV. The sharp ring structure indicates that all of these ionization processes occur with the vibrational selection rule $\Delta v = 0$ via intermediate Rydberg states at the energy of $\omega_1 + \omega_2$. Strong anisotropy in the photoelectron image also points to atomic-like electron orbitals in the intermediate states. The Rydberg states contributing to the two outer rings were assigned to the 3*s* ($^1A_g$) and 3*p* ($^1B_{3u}$ or $^1B_{2u}$) Rydberg states. The time dependencies of photoelectron intensity for the three rings are shown in Figure 1(b). The two outer distributions decay as a function of time ($\tau$ = 110 ps), while the inner one grows with the same time constant, corresponding to the intersystem crossing from the $S_1$ to the triplet manifold.

We have analyzed these revival features based on the theory of RCS reported by Felker and Zewail.[1)] For simplicity, we approximated the $S_1$ state of pyrazine as an oblate symmetric top. By assuming the transitions from $S_1$ to $R_n{}^{3s}$ and to $R_n{}^{3p}$ to be parallel and perpendicular, respectively, simulation of the RCS revivals agrees almost perfectly with observation, as shown in Figure 2(b). The transition from the $S_1$ ($^1B_{3u}$) to the 3*p* ($^1B_{3u}$ or $^1B_{2u}$) state is vibronically induced by excitation of the mode 11 ($b_{3u}$), making the transition a perpendicular type.

The PAD measured at each time delay was fit to the following form:

$I(\theta) = \beta_{00}Y_{00}(\theta) + \beta_{20}Y_{20}(\theta) + \beta_{40}Y_{40}(\theta) + \beta_{60}Y_{60}(\theta)$,

where $Y_{LM}$ are spherical harmonics. We found $\beta_{60}$ to be negligible. The ratio $\beta_{20}/\beta_{00}$ thus obtained for ionization of $S_1$ via the 3*s* and 3*p* Rydberg states also clearly shows the rotational revivals [Figure 1(c)]. In the present case, the pump pulse creates a time-dependent alignment $A_{20}(t)$ in the $S_1$ state, and the probe pulse transfers this alignment to rotational levels in the Rydberg states. Since these states are ionized instantaneously within a probe laser pulse, the PAD is modulated only by the time dependence of $A_{20}(t)$ in the $S_1$ state.

**Reference**

1) P. M. Felker, J. S. Baskin and A. H. Zewail, *J. Phys. Chem.* **90**, 724 (1986).

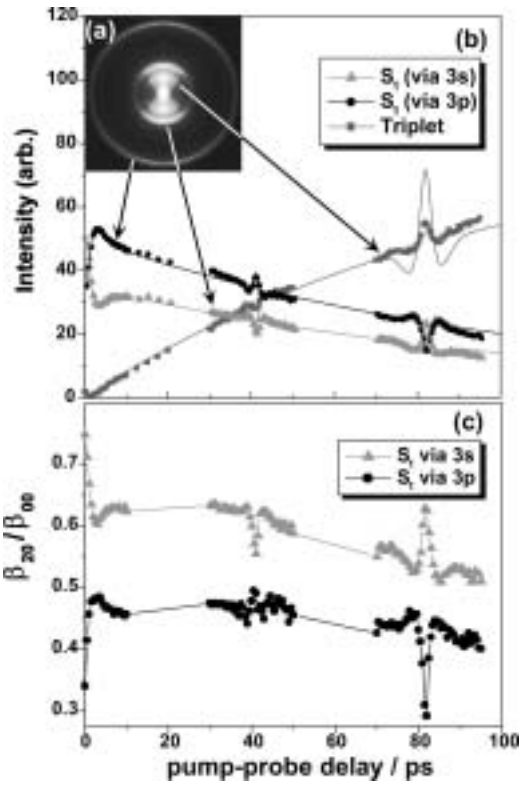


**Figure 1.** (a) Inverse Abel transformed photoelectron image of the [1+2'] PEI of pyrazine via the $S_1$ $B_{3u}(n\pi^*)$ $0^0$ level observed at the time delay of 30 ps. The original image was integrated 80 000 laser shots. (b) Time evolution of three major components in the [1+2'] PEI. Circle (●), triangle (▲), and square (■) represent the angle integrated intensity for the outer (KE = 643 meV), middle (101 meV), and inner ring (37 meV), respectively. Solid lines are a simulation taking into account the rotational coherence. (c) $\beta_{20}/\beta_{00}$ as a function of pump-probe time delay in the [1+2'] PEI.

## III-H-2 Femtosecond Photoelectron Imaging on Pyrazine: Spectroscopy of 3*s* and 3*p* Rydberg States

**SONG, Jae Kyu[1]; TSUBOUCHI, Masaaki[2]; SUZUKI, Toshinori**
*([1]Seoul Natl. Univ.; [2]GUAS)*

[*J. Chem. Phys.* **115**, 8810 (2001)]

Femtosecond two-color and one-color photoelectron imaging have been applied to Rydberg states (n = 3) of jet-cooled Pyrazine. The 3s and 3p members of Rydberg series converging to the ground state ($n^{-1}$) of the cation and the 3s member of Rydberg series converging to an excited state of the cation ($\pi^{-1}$) were observed. Figure 1 (a) shows (2+1) REMPI spectrum of jet-cooled Pyrazine observed with our tunable femtosecond laser. There are two band systems. The first system exhibits a progression of the 6a mode, indicating the geometry change from $S_0$ along this mode. The second system does not indicate such a prominent geometry change. Figure 1 (b) is the He(I) photoelectron spectrum of Pyrazine adopted from the literature.[1)] Here, the first system is the ground state ($^2A_g$) of the cation and the second system is the excited state ($^2B_{1g}$) of the cation. The spectral features in Figure 1 (a) and (b) are remarkably similar, from which the two systems in Figure 1 (a) are assigned to 3($n^{-1}$) and 3s($\pi^{-1}$) Rydberg states. The energy difference between the 3s($\pi^{-1}$) and 3s($n^{-1}$) Rydberg states is 820 meV, while the energy difference between $I_0(^2A_g)$ and $I_1(^2B_{1g})$ is 880 meV. The quantum defects calculated for the 3s($\pi^{-1}$) and 3s($n^{-1}$) Rydberg states are 0.87 and 0.86, respectively. The difference in electronic character between the 3s($\pi^{-1}$) and the 3s($n^{-1}$) Rydberg states was also evident in the photoelectron angular distributions for ionization out of these orbitals.

The spectrum shown in Figure 1(b) is strikingly different from the one reported by Turner *et al.* using a nanosecond laser[2)] in that (1+2) REMPI spectrum via $T_1$ is completely missing in our data. This is presumably because the ionization efficiency of the rapidly-decaying Rydberg states was substantially lower with nanosecond lasers, making the $T_1 \leftarrow S_0$ spectrum more dominant.

The Franck-Condon factors in electronic transitions involving $S_0$, $S_1$, $S_2$, 3s($n^{-1}$), 3s($\pi^{-1}$), $D_0$, and $D_1$ were analyzed to examine conical intersections between these states, and the intersection was identified between $S_1$-$S_2$, 3s($n^{-1}$)-3s($\pi^{-1}$) and $D_0$-$D_1$. Although the electronic dephasing times for $S_2$-$S_1$ and $D_1$-$D_0$ have been estimated to be 30 fs, the photoelectron angular distribution indicated that 3s($n^{-1}$)-3s($\pi^{-1}$) dephasing is not completed within 100 fs.

**References**

1) H. Fridh, L. Asbrink, B. O. Jonsson and E. Linddholm, *Int. J. Mass Spectrom.* **8**, 101 (1972).
2) R. E. Turner, V. Vaida, C. A. Molini, J. O. Berg and D. H. Parker, *Chem. Phys.* **28**, 47 (1978).

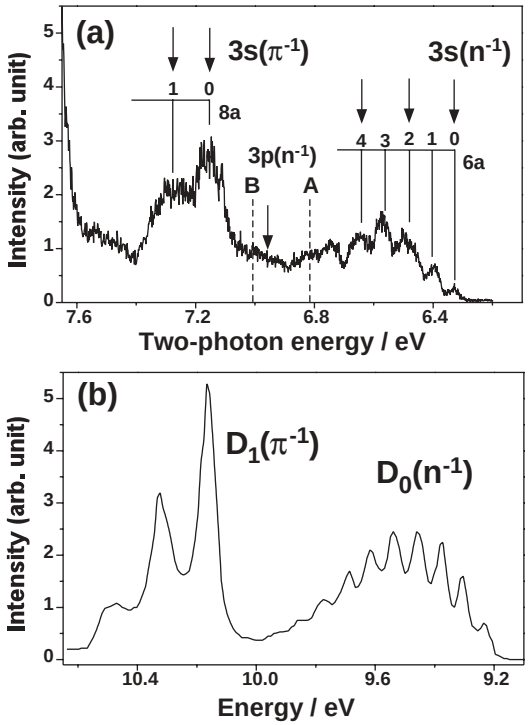


**Figure 1.** (a) One-color REMPI spectrum in the 325–400 wavelength region. The abscissa of the spectrum represents the two-photon energy in eV. The assignments of the vibrational progressions are indicated in the figure. The origins of 3pA and 3pB Rydberg states, although they are not visible in the spectrum, are indicated by broken lines. (b) He (I) photoelectron spectrum of Pyrazine shown on the same scale as (a). Adopted from reference 1.

## III-H-3 Photoionization Dynamics of CO Studied by Photoelectron Imaging

**KATAYANAGI, Hideki; MATSUMOTO, Yoshiteru; DE LANGE, Cornelis A.; SUZUKI, Toshinori**

The photoelectron energy and angular distributions in (2+1) REMPI of CO via the $B^1\Sigma^+$ ($v'$ = 0 and 1) states have been observed by photoelectron imaging. Jet-cooled CO molecule was ionized using UV light near 230 nm, and the photoelectrons were projected onto a position-sensitive imaging detector.

Since the $B^1\Sigma^+$ ($v'$ = 0) state is the 3s member of a Rydberg series converging to the $X^2\Sigma^+$ ($v^+$) state of $CO^+$, the $\Delta v$ = 0 propensity rule may be anticipated. However, off-diagonal transitions, $\Delta v$ = 1–7, were observed. Figure 1 shows the observed photoelectron image. Two outer rings with strong intensity arise from $\Delta v$ = 0 and 1 transitions corresponding to the photoelectron kinetic energy of 2.15 and 1.88 eV, respectively. In addition, close examination reveals that there are weak inner rings due to $\Delta v$ = 2–7 transitions. The rings were separated by about 260 meV in energy. These results are in agreement with a previous work by Sha *et al.*[1)] The photoelectron angular distribution exhibited high anisotropy for $v^+$ = 0 and a low value for $v^+$ = 1–7, which suggests different ionization mechanisms between the $\Delta v$ = 0 and $\Delta v$ = 1–7 ionization processes. The latter, off-diagonal transitions, are

ascribed to autoionization from a superexcited Rydberg state converging to the first excited ionic state ($A^2\prod$).

In the photoelectron spectrum via $B^1\Sigma^+$ ($v'$ = 1) state, the $\Delta v$ = 0 transition was dominant, which is different from the spectrum via $B^1\Sigma^+$ ($v'$= 0).

**References**

1) G. Sha, D. Proch, Ch. Rose and K. L. Kompa, *J. Chem. Phys.* **99**, 4334 (1993).

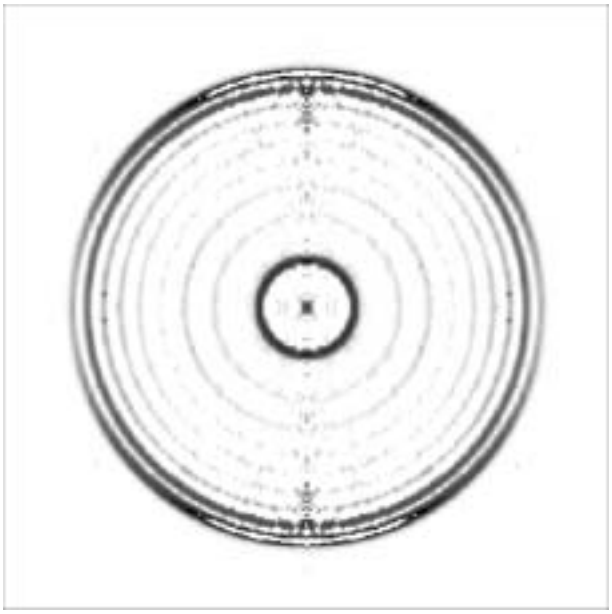

**Figure 1.** Inverse Abel transformed (512 × 512 pixels) photoelectron image of [2+1] REMPI of CO via the $B^1\Sigma^+$ ($v'$ = 0) state. The original image was integrated for 90,000 laser shots.

# III-I Bimolecular Reaction Dynamics

Chemical reactions under thermal conditions occur with various collision energies, internal quantum states, and impact parameters. The experimental data measured under such conditions are highly-averaged quantities, from which detailed feature of reactions can hardly be learned. A crossed molecular beam method allows us to observe chemical reactions of state-selected reagents at well-defined collision energy. The differential cross section (angular distribution of products) reveals impact-parameter dependence of reaction probability and reaction mechanism.

## III-I-1 Differential Cross Sections for the Inelastic Scattering of NO ($X^2\prod_\Omega$) by Ar Studied by Crossed Molecular Beam Ion-Imaging and Quantum Scattering Calculations

**KOHGUCHI, Hiroshi; SUZUKI, Toshinori; ALEXANDER, H. Millard[1]**
*([1]Univ. Maryland)*

[*Science* **294**, 832 (2001)]

High-resolution ion-imaging combined with a crossed molecular beam method has been applied to the state-resolved differential cross sections (SR-DCSs) of inelastic scattering of NO ($j$" = 0.5, Ω" = 1/2) + Ar → NO ($j$', Ω' = 1/2, 3/2) + Ar at a collision energy of 516 $cm^{-1}$. Sensitive ($j$', Ω')-dependence and complex undulations of the obtained SR-DCS were investigated by comparison with rigorous theoretical calculations. The close-coupling scattering calculation without any dynamical approximation based on the two ab initio potential energy surfaces [CEPA and CCSD(T) calculations] were carried out for the theoretical SR-DCS. The above quantum features observed in the ΔΩ = 0 scattering were almost completely reproduced by the two *ab initio* surfaces consistently. Noticeable discrepancy between the two calculations, although the CCSD(T) potential energy surfaces yielded the better agreement with the experiment, was seen in the forward scattering of the middle Δ$j$ in the ΔΩ = 1 transitions. The major difference between the CCSD(T) and CEPA surfaces lying in the potential well region at the T-shaped configuration resulted in these discrepancies of the specific scattering angles in the limited ($j$', Ω') states.

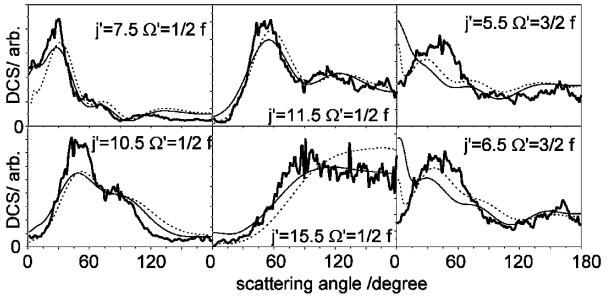


**Figure 1.** State-resolved differential cross sections of the NO + Ar inelastic scattering at the collision energy of 516 $cm^{-1}$. The initial state of the collision is $j$" = 0.5, Ω" = 1/2 state. The thick-solid lines represent the experimental differential cross sections. The thin-solid and broken lines are the theoretical results based on the CCSD(T) and the CEPA *ab initio* PESs, respectively.

# III-J Structure and Properties of Polyoxometalates with a Magnetic, Electronic, or Biological Significance

Polyoxometalates constitute model systems for the study of the electron and energy transfer in the infinite metal-oxide lattice and their simplicity allows to treat at the molecular scale the coupling of electronic and nuclear movements, which is an inherent problem for the mixed-valence systems. As is clear from such a variety of both structure and reactivity of polyoxometalates, our current works on polyoxometalates are 1) structure/reactivity relationships with particular regard to the mechanism of electron transfer reactions, 2) magnetic interaction and molecular magnetic device, 3) energy-transfer mechanism and luminescence device (including nonlinear optical device), 4) encapsulation of templates in the photo-induced self-assembly process, 5) template-exchange reaction and topology, and 6) antibacterial effects on methicillin-resistant *Staphylococcus aureus* (MRSA) and human gastric pathogen of *Helicobacter pylori*.

## III-J-1 A Highly Nuclear Vanadium-Containing Tungstobismutate: Synthesis and Crystal Structure of $K_{11}H[(BiW_9O_{33})_3Bi_6(OH)_3(H_2O)_3V_4O_{10}]\cdot 28H_2O$

**BOTAR, Bogdan; YAMASE, Toshihiro; ISHIKAWA, Eri**
*(IMS and Tokyo Inst. Tech.)*

[*Inorg. Chem. Commun.* **3**, 578 (2000)]

A novel and large heteropolyanion $[(BiW_9O_{33})_3Bi_6(OH)_3(H_2O)_3V_4O_{10}]^{12-}$ has been synthesized by reaction of sodium metavanadate with $Na_9[BiW_9O_{33}]\cdot 16H_2O$ in acetate buffer solutions (at pH 4.8). The present anion has a trilobal structure in which three α-B $[BiW_9O_{33}]$ units are connected to each other by an unique core $[Bi_6(OH)_3(H_2O)_3V_4O_{10}]^{15+}$. A central bismutate/vanadate-mixed core comprises three sets of two types of the $BiO_6$ pentagonal pyramid, the edge-sharing $VO_5$ square-pyramidal triad, and a $VO_4$ tetrahedron.

## III-J-2 Photochemical Self-Assembly Reaction of β-$[Mo_8O_{26}]^{4-}$ to Mixed-Valence Cluster $[Mo_{37}O_{112}]^{26-}$ in Aqueous Media

**YAMASE, Toshihiro; ISHIKAWA, Eri**
*(IMS and Tokyo Inst. Tech.)*

[*Langmuir* **16**, 9023 (2000)]

Prolonged photolysis of β-$[Mo_8O_{26}]^{4-}$ in the presence of electron-donative MeOH in aqueous solutions at pH 3.3 provides stepwise self-organization to paramagnetic reddish-brown mixed-valence species $[H_{14}Mo^{V}_{24}Mo^{VI}_{13}O_{112}]^{12-}$. The X-ray structural analysis of the reddish brown crystals, isolated as $[NMe_4]^+$ salt, shows that $[H_{14}Mo^{V}_{24}Mo^{VI}_{13}O_{112}]^{12-}$ anion consists of a central $T_d$ $[H_{10}(Mo^{V}_{12}O_{40})(Mo^{VI}O_2)_3]^{4-}$ core sandwiched by two $[H_2Mo^{V}_6Mo^{VI}_5O_{33}]^{4-}$ ligands, with overall symmetry of $D_{2d}$. The central $\{Mo^{V}_{12}O_{40}\}$ subcore (with six short $Mo^V$–$Mo^V$ contacts, 2.56(1) and 2.625(7) Å) is a tetrahedral ε-Keggin structure with a cavity (in the size of ~3.3 Å) accommodating four protons, and is stabilized by capture of four $\{Mo^{VI}O_2\}$ groups with 3/4 occupancy. The $\{Mo^{V}_6Mo^{VI}_5O_{33}\}$ framework as the ligand consists of two sets of a dinuclear $\{Mo^{V}_2O_4\}$ pair with a $Mo^V\cdots Mo^V$ distance of 2.567(7) Å, two sets of the edge-shared $\{Mo^{VI}_2O_{10}\}$ octahedra, and three mononuclear groups of one $Mo^{VI}O$ and two $Mo^{V}O_2$. The $Mo^V$ atoms in the two $Mo^{V}O_2$ groups in the ligand are separated with distance of 6.31(1) Å, being ESR-active ($\langle g\rangle$ = 1.909, $g_\perp$ = 1.894, and $g_{||}$ = 1.939 at 77 K). The structure of the $[H_{14}Mo^{V}_{24}Mo^{VI}_{13}O_{114}]^{12-}$ anion is slightly different from the diamagnetic species $\{[H_6Mo^{VI}_2O_{40}(Mo^{V}O_3)_4]$-$[H_3Mo^{V}_4Mo^{VI}_6O_{29}][H_5Mo^{V}_6Mo^{VI}_5O_{31}]\}^{14-}$ prepared by thermal reduction of $[Mo_7O_{24}]^{6-}$ with $N_2H_4\cdot H_2SO_4$, in both structure and mixed-valency of the ligand. The stepwise self-assembly processes from β-$[Mo_8O_{26}]^{4-}$ to $[H_{14}Mo^{V}_{24}Mo^{VI}_{13}O_{114}]^{12-}$ are discussed in terms of the photochemical multi (six- and four-) electron reduction of β-$[Mo_8O_{26}]^{4-}$ which results in the splitting into $\{Mo_4\}$, $\{Mo_2\}$, and $\{Mo_1\}$ fragments.

## III-J-3 A Spherical Potassium-Capped Vanadium Methylphosphonate as Another ε-Keggin Fragment, $[H_6KV_{12}O_{27}(VO_4)(PO_3CH_3)_3]^{5-}$

**YAMASE, Toshihiro; MAKINO, Haruyo; NARUKE, Haruo; SAN JOSÉ WÉRY, Ana Maria**
*(IMS and Tokyo Inst. Tech.)*

[*Chem. Lett.* 1350 (2000)]

An $[H_3KV_{12}O_{27}(AsO_4)_4]^{6-}$-isostructural ε-Keggin fragment anion, $[H_6KV_{12}O_{27}(VO_4)(PO_3CH_3)_3]^{5-}$, was photochemically prepared. This $K^+$-capped anion is formally built of nine $V^{IV}O_6$ octahedra, three $PO_3C$ tetrahedra, and four $V^{V}O_4$ tetrahedra, one of the latter being a central $VO_4^{3-}$ group. The capping $K^+$ cation lies on the $C_3$ axis and links two adjacent anion, to form a linear chain of the anions along c-axis.

## III-J-4 Chemical Structure and Intramolecular Spin-Exchange Interaction of $[(VO)_3(SbW_9O_{33})_2]^{12-}$

**YAMASE, Toshihiro; BOTAR, Bogdan; ISHIKAWA, Eri; FUKAYA, Keisuke**
*(IMS and Tokyo Inst. Tech.)*

[*Chem. Lett.* 56 (2001)]

The crystal structure determination of tris(vanadyl)-substituted tungstoantimonate(III) $K_{11}H[(VO)_3(SbW_9$-

$O_{33})_2]\cdot 27H_2O$ reveals that the $[(VO)_3(SbW_9O_{33})_2]^{12-}$ anion contains three exterior $VO^{2+}$ groups sandwiched by two α-B $[SbW_9O_{33}]^{9-}$ ligands in $V^{IV}\cdots V^{IV}$ separation of 5.411(8)–5.464(8) Å and is stabilized by equatorial three $K^+$ ions triangle with virtual $D_{3h}$ symmetry. An observable spin-exchange interaction between $V^{IV}$ centers within the vanadyl coplanar triangle is demonstrated in terms of $S = 1/2$ and $S = 3/2$ states.

### III-J-5 Synthesis and Structure of $Ln(W_5O_{18})$-Capped Mixed-Ligand Polyoxotungstolanthanoate $[Ln(W_5O_{18})\{Ln(H_2O)_2(SbW_9O_{33})(W_5O_{18})\}]^{15-}$ (Ln = Sm and Er)

**NARUKE, Haruo; YAMASE, Toshihiro**
*(IMS and Tokyo Inst. Tech.)*

[*Bull. Chem. Soc. Jpn.* **74**, 1289 (2001)]

Polyoxotungstolanthanoate, $[Ln_2(H_2O)_2(SbW_9O_{33})(W_5O_{18})_2]^{15-}$ (Ln = Sm and Er), possessing $Ln^{3+}$, trivacant α-B-Keggin $[SbW_9O_{33}]^{9-}$, and monovacant Lindqvist $[W_5O_{18}]^{6-}$ groups with a ratio of 2:1:2, was prepared and structurally characterized. In the anion the α-B-$[SbW_9O_{33}]^{9-}$ group coordinates to two $[Ln(W_5O_{18})]^{3-}$ moieties through terminal- and bridging-O atoms at vacant and non-vacant sites, respectively. A $^{183}W$-NMR spectrum for $Y^{3+}$-analog in aqueous solution was consistent with this anion structure.

### III-J-6 Three-Dimensional Inorganic/Organic Hybrid Material, $[Ni_2(4,4'\text{-bipy})_3(H_2O)_2V_4O_{12}]\cdot 2.5H_2O$

**YANG, Lan; HU, Changwen; NARUKE, Haruo; YAMASE, Toshihiro**
*(IMS and Tokyo Inst. Tech.)*

[*Acta Crystallogr., Sect. C: Cryst. Struct. Commun.* **57**, 799 (2001)]

The title compound has been prepared by hydrothermal method and characterized by elemental analysis, IR spectroscopy, and single-crystal X-ray diffraction. The structure consists of $\{V_2O_6\}$, $\{Ni(1)(4,4'\text{-bipy})_4O_2\}$ and $\{Ni(2)(H_2O)_2(4,4'\text{-bipy})_2O_2\}$ polyhedra, and water molecules of crystallization. The Ni atoms and one bipyridyl group lie on centers of symmetry.

### III-J-7 Molecular Aspect of Energy Transfer from $Tb^{3+}$ to $Eu^{3+}$ in Polyoxometalate Lattices: An Approach for Molecular Design of Rare-Earth Metal-Oxide Phosphors

**YAMASE, Toshihiro**
*(IMS and Tokyo Inst. Tech.)*

[*Polyoxometallates: From Topology to Industrial Applications* M. T. Pope and A. Müller, Eds., Kluwer Academic Publishers, pp. 187–203 (2001)]

The exploitation of mixed heteronuclear rare-earth-element-containing polyoxometalates to probe the multipolar nature of heteronuclear rare-earth interactions is imaginative. It appears that polyoxometallolanthanoates are ideal for this type of investigation. Three structural types of $Tb^{3+}/Eu^{3+}$ heterolanthanide-multinuclear polyoxometalates, $K_{15}H_3[Tb_{1.4}Eu_{1.6}(H_2O)_3(SbW_9O_{33})(W_5O_{18})_3]\cdot 25.5H_2O$, $Na_7H_{19}[Tb_{4.3}Eu_{1.7}O_2(OH)_6(H_2O)_6Al_2(Nb_6O_{19})_5]\cdot 47H_2O$, and $[NH_4]_{12}H_2[Tb_{3.1}Eu_{0.9}(MoO_4)(H_2O)_{16}(Mo_7O_{24})_4]\cdot 13H_2O$ are studied by crystal structures, emission and excitation spectra, and emission decay dynamics. The excitation of the $Tb^{3+}$ $^7F_6 \rightarrow {}^5D_4$ transitions produces not only the emission lines of $Tb^{3+}$, but also those of $Eu^{3+}$, accompanied by nonexponential rise and decay curves of the emission from $Tb^{3+}$ and $Eu^{3+}$. There is no significant exchange interaction between the lanthanide ions, as a result of the coordination of aqua and/or hydroxo ligands to the lanthanide ions. The mechanism of the $Tb^{3+} \rightarrow Eu^{3+}$ energy transfer is identified as a Förster-Dexter-type energy transfer from $Tb^{3+}$ (donor) to $Eu^{3+}$ (acceptor). The nearest-neighbor energy-transfer rates by electric dipole-dipole interactions between a Tb-Eu pair at 4.2 K are estimated to be $4.5 \times 10^4$, $4.7 \times 10^5$, and $4.9 \times 10^3$ $s^{-1}$ and the critical radii at 4.2 K are 10.3, 10.0, and 6.17 Å for $K_{15}H_3[Tb_{1.4}Eu_{1.6}(H_2O)_3(SbW_9O_{33})(W_5O_{18})_3]\cdot 25.5H_2O$ (with Tb-Eu separation of 5.05 Å), $Na_7H_{19}[Tb_{4.3}Eu_{1.7}O_2(OH)_6(H_2O)_6Al_2(Nb_6O_{19})_5]\cdot 47H_2O$ (with 3.76 Å separation), and $[NH_4]_{12}H_2[Tb_{3.1}Eu_{0.9}(MoO_4)(H_2O)_{16}(Mo_7O_{24})_4]\cdot 13H_2O$ (with 6.17 Å separation), respectively. The low symmetry ($C_s$ or $C_1$) of the $LnO_8$ (Ln = Tb and Eu) coordination polyhedra allows the nonvanishing electric-dipole transition probability for the $^7F_J \leftrightarrow {}^5D_0$ ($J = 0, 1$) transitions which leads to a faster transfer rate at high temperatures. The photoexcitation of the host lattices (tungstate, niobate, and molybdate) induced the energy transfer from the oxygen-to-metal charge-transfer {O → M (= Nb, Mo, W) lmct} triplet states to $Tb^{3+}$ ($^7F_6 \rightarrow {}^5D_4$) and $Eu^{3+}$ ($^7F_{0,1,2} \rightarrow {}^5D_{0,1}$). In the case of $[NH_4]_{12}H_2[Tb_{3.1}Eu_{0.9}(MoO_4)(H_2O)_{16}(Mo_7O_{24})_4]\cdot 13H_2O$ this transfer is not complete and the O → Mo lmct triplet emission of molybdates is observed to provide the rate constant for the energy transfer to $Tb^{3+}/Eu^{3+}$ sites with $4.4 \times 10^6$ $s^{-1}$.

# III-K Structure and Exited-State Dynamics of Aromatic Clusters

Clusters containing aromatic molecules are model systems for elucidating intermolecular interactions that control macroscopic properties of the molecules in condensed phases, such as liquids and crystals. We focus on detailed correlation of dynamical behavior of photo-excited aromatic chromophore to geometry and bonding topology of the clusters. Especially, it is critically important to definitely characterize the cluster structure, and we implement various laser-based methods, such as IR–UV double resonance and rotational coherence spectroscopy (RCS), in conjunction with molecular-orbital calculations. The following subjects have been studied; 1) hydrogen-bonding networks and nonradiative dynamics of a bi-functional aromatic solvated by water molecules, 2) experimental determination of solvation structure of aromatic clusters by RCS, and 3) reexamination of electronic spectra of $(benzene)_n$ clusters.

## III-K-1 Electronic Spectroscopy of 9(10H)-Acridone and Its Hydrated Clusters

**MITSUI, Masaaki[1]; OHSHIMA, Yasuhiro[1,2]**
*([1]Kyoto Univ.; [2]IMS)*

[*J. Phys. Chem. A* **104**, 8638 (2000)]

The lowest $^1(\pi,\pi^*)$ electronic transition of 9(10H)-acridone (AD) and its hydrated clusters has been studied by fluorescence-based laser spectroscopy and mass-selective two-color resonance-enhanced two-photon ionization (2C-R2PI). Thirteen fluorescent hydrates as well as the monomer have been identified in fluorescence-excitation and UV–UV hole-burning measurements, and size assignments for relatively smaller clusters, $AD–(H_2O)_n$ ($n$ = 1–6), have been conducted by 2C-R2PI. The origin bands for larger-size clusters show larger red shifts converging at *ca.* 2200 $cm^{-1}$, but the changes are non-monotonic with a substantial increase from $n$ = 2 to 3. DFT calculations at the B3LYP/6–31G(d,p) level have predicted that the energy difference between the C=O and N–H bonded isomers is quite small (only ≈ 1 kcal/mol) for $n$ = 1 and 2. The observed spectral shifts of fluorescent hydrates with $n$ = 1 and 2 are well reproduced by the HOMO–LUMO gap in the calculated orbital energies of either of the N–H or C=O bonded isomers, leaving the definitive structural assignments to fluorescence-detected infrared spectroscopy described in the next section. For the larger clusters ($n$ = 3–5), several minimum-energy structures have been identified within 2 kcal/mol in binding energy, among which the conformers with water molecules bridging between the C=O and N–H sites over the AD's aromatic rings are identified as the observed species, based on good agreement between the calculated and observed spectral shifts.

## III-K-2 Characterization of Hydrogen-Bonding Networks in 9(10H)-Acridone and Its Hydrated Clusters

**MITSUI, Masaaki[1]; OHSHIMA, Yasuhiro[1,2]; ISHIUCHI, Shun-ichi[3]; SAKAI, Makoto; FUJII, Masaaki**
*([1]Kyoto Univ.; [2]IMS; [3]GUAS)*

[*J. Phys. Chem. A* **104**, 8649 (2000)]

Fluorescence-detected infrared measurements have been performed for 9(10H)-acridone (AD) and ten of its fluorescent hydrated clusters, $AD–(H_2O)_n$ ($n$ = 1–5 and more). In the $n$ = 1 and 2 clusters, free N–H stretching band has been identified in addition to O–H stretching bands characteristic to water molecules acting as single proton donors. As the next solvation step, the H-bonded O–H stretches are further developed in the red-shifted region and the N–H stretch becomes involved in the hydrogen-bonds for the n = 3–5 clusters. For $n \geq 6$, more than one pair of double-donor O–H stretches come to appear. These spectral features are well correlated to the stepwise evolution in the hydrogen-bonding networks in $AD–(H_2O)_n$, which have been predicted by the $(\pi,\pi^*)$ spectral-shift analysis and DFT calculations presented in the above section: waters units are bound to the C=O site for $n$ = 1 and 2, a single water chain bridges between the C=O and N–H sites above the AD's aromatic rings for $n$ = 3–5, and water bridges become branched for $n \geq 6$ and probably form three dimensional cages at higher aggregation level.

## III-K-3 Microscopic Solvation Effects on Nonradiative Dynamics in 9(10H)-Acridone and Its Hydrated Clusters

**MITSUI, Masaaki[1]; OHSHIMA, Yasuhiro[1,2]; KAJIMOTO, Okitsugu[1]**
*([1]Kyoto Univ.; [2]IMS)*

[*J. Phys. Chem. A* **104**, 8660 (2000)]

Nonradiative dynamics and energy-level structure of relevant electronic excited states in 9(10H)-acridone (AD) and its hydrated clusters have been studied. The fluorescence decay is very fast (≈ 10 ps) for bare AD but drastically lengthened (> ns) in the clusters. Bare AD has been observed by delayed ionization and sensitized phosphorescence, which indicates the efficient formation of molecules in triplet manifold after the $^1(\pi,\pi^*)$ excitation. Several weak peaks attributable to $^3(n,\pi^*)$ transitions are identified in bare AD, but such satellites completely disappear in the fluorescent cluster spectra with $n \geq 1$. The dominant nonradiative pathway in bare AD is the $S_1(\pi,\pi^*) \rightarrow T_2(n,\pi^*)$ intersystem crossing (ISC) followed by the $T_2(n,\pi^*) \rightarrow T_1(\pi,\pi^*)$ internal conversion. This direct ISC process becomes prohibited by the energy-level inversion between $S_1$ and

$T_2$ induced by the H-bonding to the C=O site. The relaxation pathway is switched to the second-order ISC [$S_1(\pi,\pi^*) \rightarrow T_1(\pi,\pi^*)$] in the fluorescent hydrated clusters, where the carbonyl site is H-bonded. Owing to the increasing $S_1$–$T_2$ separation, the fluorescence quantum yield becomes larger for the higher clusters, which is approaching to the bulk solution value. A small fall-off in the decay constants from $n$ = 2 to 3 is correlated to the crossover in H-bonding topologies (the C=O bonded → the bridged form), which has been established in the above sections. The delayed ionization has identified new spectral features that are absent in the fluorescence excitation spectrum. They are assigned to the N–H bonded isomer(s) with $n \leq 3$, in which the ISC should be as fast as in bare AD because of the lack of the $S_1$–$T_2$ level inversion. These experimental findings demonstrate the site-specific solvation effects on the nonradiative dynamics in the hydrated clusters of AD.

### III-K-4 Structural Characterization of 9-Cyanoanthracene–(Ar)$_n$ ($n$ = 0–3)

**EGASHIRA, Kazuhiro[1]; OHSHIMA, Yasuhiro[1,2]; KAJIMOTO, Okitsugu[1]**
*([1]Kyoto Univ.; [2]IMS)*

[*J. Phys. Chem. A* **105**, 1131 (2001)]

Rotational coherence spectroscopy implemented with time-resolved fluorescence depletion has been applied in a structural study of 9-cyanoanthracene (CNA) and its clusters with Ar up to three atoms. For bare CNA, *C*-type transients for the $S_1$ and $S_0$ states have been observed separately, yielding independent sets of rotational constants for the two states. For the Ar clusters, rotational constants as averages for $S_1$ and $S_0$ have been derived to fix the cluster geometry. The Ar atom in CNA–Ar is located 3.46 ± 0.03 Å above the central aromatic ring of CNA and displaced slightly from the ring center toward the cyano group. The plane–Ar distance is quite close to those in clusters with other polycyclic aromatic molecules. Two values (≈ 0.2 or 0.6 Å) for the displacement to the cyano group are consistent with the experimental data, and results on related aromatics–Ar show that the former is preferable. The dominant conformer of CNA–$(Ar)_2$ has been determined as a two-sided (1 + 1) type: structures for each sides of the CNA plane are the same as that of CNA–Ar within the experimental uncertainties. CNA–$(Ar)_3$ has a (2 + 1)-type structure: one side of the substrate is the same as CNA–Ar and an Ar dimer lies 3.48 ± 0.04 Å above the other side. The determined conformations of CNA–$(Ar)_{1,3}$ are the same as the corresponding anthracene clusters, but that of CNA–$(Ar)_2$ is in contrast to anthracene–$(Ar)_2$, which has been identified as a (2 + 0) type. Model potential calculations have been employed to explain the difference in structural motifs of the two closely related clusters.

### III-K-5 Structural Characterization of 9-Cyanoanthracene–Water

**EGASHIRA, Kazuhiro[1]; OHSHIMA, Yasuhiro[1,2]; KAJIMOTO, Okitsugu[1]**
*([1]Kyoto Univ.; [2]IMS)*

[*Chem. Phys. Lett.* **334**, 285 (2001)]

Rotational coherence spectroscopy has been applied to determine rotational constants of the two isotopic species of the 9-cyanoanthracene–water complex, CNA–$H_2O$ and CNA–$D_2O$. To support the experimental observation DFT calculations [B3LYP/6-31G(d,p)] have been also performed to identify several stable conformations. The structure of the complex is found to be such that water is hydrogen-bonded to the π-electrons of the cyano group of CNA. Geometrical parameters consistent with the experimental results are evaluated.

### III-K-6 Structural Characterization of 1:1 van der Waals Complexes of 9-Cyanoanthracene with Aprotic Solvents

**EGASHIRA, Kazuhiro[1]; OHSHIMA, Yasuhiro[1,2]; KAJIMOTO, Okitsugu[1]**
*([1]Kyoto Univ.; [2]IMS)*

[*J. Phys. Chem. A* **105**, 4781 (2001)]

Structures of 9-cyanoanthracene (CNA) clusters microsolvated with single molecule of aprotic solvents (carbon dioxide, two isotopomers of acetonitrile, and fluoroform) have been studied by rotational coherence spectroscopy. All the observed traces exhibit pronounced *C*-type transients, which suggests that these species are quite close to planar asymmetric tops with their electronic transition moments pointing to in-plane directions. Weak *J*-type transients have been also identified for CNA–$CO_2$ and –$CF_3H$, latter of which shows *A*-type transients in addition. By comparing the experimental observations with B3LYP/6-31G(d,p) calculations, it is concluded that the solvent molecule is located by the side of the CN group of CNA with its molecular axis lying in the CNA molecular plane. All the cluster geometries are of $C_s$ symmetry, in which a positively charged atom of the solvents (C, H, or H for $CO_2$, $CH_3CN$, and $CF_3H$, respectively) is close to the cyano nitrogen of CNA, while an electonegative part (O, N, or F) contacts with the 1-position hydrogen of CNA. Some geometrical parameters including the centers of mass separation are obtained from the derived rotational constants.

### III-K-7 Size Reassignments of the $S_1$–$S_0$ Vibronic Spectra of Benzene Clusters

**IIMORI, Toshifumi[1]; OHSHIMA, Yasuhiro[1,2]**
*([1]Kyoto Univ.; [2]IMS)*

[*J. Chem. Phys.* **114**, 2867 (2001)]

The vibronic band systems of $(benzene)_n$ clusters in the $S_1$–$S_0$ vibronic region are revisited by mass-selective resonant two-photon ionization and ultraviolet–ultraviolet hole-burning spectroscopies. A detailed examination of the spectra of isotopomers with isotopic

mixture of $C_6H_6$ and $C_6D_6$ reveals that there is substantial fragmentation for $n \geq 3$ following photoionization. This observation concludes that it is necessary to correct the size assignments. Transitions which have been formerly identified to the trimer are most probably due to the tetramer. Instead, reassigned to the trimer is the band system which has been believed to be of an isomeric form of the dimer.